Geochimica et Cosmochimica Acta 385 (2024) 118–140

Contents lists available at ScienceDirect

Geochimica et Cosmochimica Acta

journal homepage: www.elsevier.com/locate/gca

A petrogenetic study of apatite in Chang'E-5 basalt: Implications for high sulfur contents in lunar apatite and volatile estimations for the lunar mantle

Huijuan Li [a,b,*], Zilong Wang [b], Zhenyu Chen [c], Wei Tian [b], Wei-(RZ) Wang [d], Guibin Zhang [b], Lifei Zhang [b]

[a] Center for High Pressure Science and Technology Advanced Research (HPSTAR), Beijing 100193, China
[b] MOE Key Laboratory of Orogenic Belts and Crustal Evolution, School of Earth and Space Sciences, Peking University, Beijing 100871, China
[c] Key Laboratory of Metallogeny and Mineral Assessment of MNR, Institute of Mineral Resources, Chinese Academy of Geological Sciences, Beijing 100037, China
[d] Key Laboratory of Paleomagnetism and Tectonic Reconstruction of MNR, Institute of Geomechanics, Chinese Academy of Geological Sciences, Beijing 100081, China

ARTICLE INFO

Associate editor: Mahesh Anand

Keywords:
Apatite
Volatile
Sulfur
Lunar mantle
Chang'E-5

ABSTRACT

Apatite is ubiquitous in lunar samples and has been used widely for estimating volatile abundances in the lunar interior. However, apatite compositional and isotopic variations within and between samples have resulted in varying and ambiguous results. Understanding apatite petrogenesis will help with both identifying the appropriate composition for volatile estimation and interpreting isotopic variations. Here we report a comprehensive petrogenetic investigation of apatite in Chang'E-5 (CE5) basaltic sample CE5C0800YJYX013GP. Apatite displays both intra-grain and inter-grain compositional variations with F and Cl contents falling in the ranges of 0.97–2.47 wt% and 0.24–1.09 wt%, respectively. These apatite compositions show relatively low F and high Cl characteristics in comparison to apatites of Apollo high-Ti and low-Ti mare basalts, but are similar to those reported for lunar meteorites LAP 04841 and MIL 05035. We discern three zoning profiles: fractional crystallization (FC)-dominated, degassing-induced and a third indicated by REE-enriched cores, which are interpreted as representing different generations of apatite. FC-dominated zoning is characterized with decreasing F and increasing Cl and S contents from core to rim; while the opposite is true for the degassing-induced zoning. Regardless of the zoning patterns, apatite Cl and S contents display positive correlations, with S contents up to ~ 3000 ppm, much higher than previous reports for Apollo samples (up to ~ 600 ppm). We demonstrate that the fractional crystallization model proposed by Boyce et al. (2014) in combination with H_2O degassing and high S contents in melt (likely at sulfide saturation) can explain these high Cl and S contents observed in CE5 apatite.

Based on the core composition of the FC-dominated zoning profile, which has the lowest incompatible element concentrations, bulk F, Cl and H_2O contents in the parental melt are estimated to be ~ 72 ± 21, ~43 ± 14 and ~ 1576 ± 518 ppm, respectively. These estimates have lower F/Cl ratios than those measured in olivine-hosted melt inclusions from Apollo mare basalts. By adopting the petrogenetic model for CE5 basalt proposed by Su et al. (2022), i.e., 10 % partial melting of a hybrid mantle source, followed by ~ 30–70 % fractional crystallization (~50 % for our sample), we estimate the F, Cl, H_2O and S contents in the mantle source are in the ranges of ~ 2.5–4.6, ~0.7–1.4, ~53–105 and ~ 38–125 ppm, respectively, similar to estimates for both depleted Earth mantle and primitive lunar mantle. However, by adopting the model of Tian et al. (2021), 2–3 % partial melting of a mantle source composed of 86 PCS+2% TIRL (PCS, percent crystallized solid; TIRL, trapped instantaneous residual liquid), followed by 43–88 % fractional crystallization, these estimates will be 5–10 times lower. To be certain whether the relatively low F and high Cl characteristics of CE5 apatite imply an enriched mantle source requires further evaluation of the petrogenetic models for CE5 basalt.

1. Introduction

Knowledge of the volatile budget for the lunar mantle and bulk silicate Moon provides important constraints for constructing Earth-Moon formation models and our understanding of the evolutional history of the Moon. Apatite is a ubiquitous volatile bearing mineral in

---

* Corresponding author.
E-mail address: huijuan.li@hpstar.ac.cn (H. Li).

https://doi.org/10.1016/j.gca.2024.09.002
Received 9 October 2023; Accepted 2 September 2024
Available online 4 September 2024

lunar samples and can contain F, Cl and H_2O in weight percent levels, which has played a key role in estimating the F, Cl and H_2O contents in lunar magmas and their mantle sources. However, the resulting estimations vary in quite large ranges, for example, H_2O contents in lunar mantle vary from a few ppm to more than 100 ppm, F contents from 0.56-20 ppm and Cl contents from 0.9-6 ppm (McCubbin et al., 2015b). In part, this reflects the diverse samples studied, suggesting heterogeneous volatile distributions in the lunar mantle (McCubbin et al., 2011; Robinson and Taylor, 2014). Additionally, apatite displays intra-grain and inter-grain compositional heterogeneity even within the same sample (Greenwood et al., 2011; Barnes et al., 2013; Tartèse et al., 2013; Barnes et al., 2016; Barnes et al., 2019). For example, apatites from high-Ti mare basalts have 2.69–3.75 wt% F and 0.02–0.62 wt% Cl; for low-Ti mare basalts, the F and Cl contents in apatite vary in ranges of 1.86–3.76 wt% and 0.01–0.60 wt% respectively (McCubbin et al., 2010b; Greenwood et al., 2011; McCubbin et al., 2011; Barnes et al., 2013; Tartèse et al., 2013; Boyce et al., 2015; Barnes et al., 2016; Barnes et al., 2019); and apatites from high-Al mare basalts are F-rich with 2.95–3.52 wt% F and 0.13–1.61 wt% Cl (McCubbin et al., 2010a; Boyce et al., 2010; Greenwood et al., 2011; Pernet-Fisher et al., 2014; Boyce et al., 2014; McCubbin et al., 2015b; Potts et al., 2018). Apatites from KREEP basalts have F contents of 1.52–3.76 wt% and Cl contents of 0.01–1.22 wt% (McCubbin et al., 2010a; McCubbin et al., 2011; Tartèse et al., 2014b; Barnes et al., 2016; Wang et al., 2019), spanning a similar range to low-Ti mare basalt, but with higher Cl contents.

The stable isotopic compositions of volatiles in apatite are important tools for constraining the origin and evolution of lunar volatiles. They also display large ranges within and between samples. For example, apatite from low-Ti and high-Ti mare basalts have δD values mostly in the range of + 200 ‰ to + 1100 ‰ with high δD values normally explained as the result of degassing during magma eruption (Greenwood et al., 2011; Barnes et al., 2013; Tartèse et al., 2013; Barnes et al., 2019). Apatite δ^{37}Cl values range from + 2 ‰ to + 19 ‰ for low-Ti and high-Ti mare basalts (Sharp et al., 2010; Boyce et al., 2015; Barnes et al., 2016; Barnes et al., 2019), while values are higher for KREEP basalts, +9-+31 ‰ (Sharp et al., 2010; Tartèse et al., 2014a; Barnes et al., 2016; Wang et al., 2019). There has been a debate regarding the high δ^{37}Cl values in apatite, which has been explained by the process of degassing during lunar basalt eruption and crystallization (Sharp et al., 2010; Gargano et al., 2020; Ji et al., 2022), or interpreted to represent the contribution of urKREEP (Boyce et al., 2015; Barnes et al., 2016; Barnes et al., 2019; Stephant et al., 2019). An evolution towards fluorapatite endmember during degassing has been suggested for lunar apatite based on experimentally observed volatile degassing trends in lunar magma and apatite-melt volatile partitioning data (Ustunisik et al., 2011; Ustunisik et al., 2015).

Boyce et al. (2014) proposed that the variations of apatite composition can be explained by the fractional crystallization process, that is, decreasing F content in apatite is accompanied by increasing Cl, H_2O and other nonvolatile incompatible elements, e.g., SiO_2 and rare earth elements (REEs). Such a prediction is consistent with core-to-rim zoning observed in large apatite grains from Apollo 12 basalt 12039,42, Apollo 11 basalt 10044,644 (Greenwood et al., 2011), and Apollo 14 basalt 14053,16 (McCubbin et al., 2010a). Based on their fractional crystallization model for apatite volatile compositions, Boyce et al. (2014) proposed that increasing H_2O and Cl contents in apatite during fractional crystallization are a result of F depletion in melt due to the strong preference of apatite for F over other volatiles, and meanwhile, apatite composition is constrained by stoichiometry, that is, mole fractions of F, Cl and OH add up to 1. In other words, high H_2O and Cl contents in apatite do not necessarily indicate corresponding high concentrations in melt, which has been termed “the lunar apatite paradox”. Publication of this work has greatly dampened the enthusiasm of using apatite to infer volatile abundances in the lunar mantle. As suggested by Boyce et al. (2014), apatite compositions with the lowest H_2O content in a sample may be used for volatile estimation in the parental melt. In this case, apatite compositions support the drier end of the estimations for H_2O in the lunar mantle and bulk silicate moon (BSM), e.g., 1.2–14 ppm in the BSM has been estimated based on F/H_2O ratio in apatite by McCubbin et al. (2023). However, apatite compositions are also affected by degassing, which will lead to decreasing H_2O and increasing F contents. Considering the variation of apatite compositions among different lunar basalt types, how to relate apatite composition to the heterogeneous distribution of volatiles in the lunar mantle is still an important scientific question. Distinguishing or disentangling the effects of fractional crystallization and degassing on apatite composition is essential for choosing appropriate apatite composition for volatile estimation and interpreting stable isotopic observations.

In recent years, the origin of high S contents in lunar apatite (up to ~ 600 ppm reported in Apollo samples) has become a point of contention (Konecke et al., 2017; Brounce et al., 2019; Brounce et al., 2020). Experimental studies have shown that S is incompatible in apatite under reduced conditions, with partition coefficients of 0.38 ± 0.09 and 0.02 ± 0.01 obtained at 1000 °C, 300 MPa and FMQ-1, for apatite in equilibrium with a hydrous rhyolitic melt (Konecke et al., 2017) and a hydrous lamproitic melt (Konecke et al., 2019), respectively. However, based on paired apatite-felsic glass measurements in the lunar basalt sample 12039,4, Brounce et al (2019) estimated the average value for S partition coefficients to be ~ 2 ± 1. Deciphering the S record in apatite provides additional information regarding the petrogenesis of apatite and the behavior of volatiles during lunar basaltic evolution.

On Dec 17, 2020, China’s Chang’E-5 (CE5) mission brought back 1.731 kg of lunar soil, collected from the landing site at 43.06°N, 51.92°W in the northern Oceanus Procellarum, belonging to a young mare basalt unit Em4 (the fourth Eratosthenian-aged mare unit in the region) (Qian et al., 2018). Radiometric dating of CE5 basaltic fragments (Che et al., 2021; Li et al., 2021) have confirmed its young age (~2 Ga). Thus, CE5 samples provide an opportunity to study the late stage magmatism on the Moon and enable us to gain insights into lunar mantle conditions at ~ 2 Ga. Based on analyses of apatite from a set of 23 CE5 basaltic clasts and fragments using nanoscale secondary ion mass spectrometer (NanoSIMS), Ji et al. (2022) reported F, Cl and H_2O contents in apatite varying in large ranges of 0.91–3.93 wt%, 820–11989 ppm and 134–6564 ppm respectively. There have also been reports of apatite compositions with S contents up to ~ 2000 ppm in CE5 basalts (Che et al., 2021; Hu et al., 2021; Li et al., 2021).

Here we report a detailed petrogenetic study of apatite in CE5 basaltic sample CE5C0800YJYX013GP allocated by the China National Space Administration (CNSA). The effects of fractional crystallization, degassing, sulfide saturation and melt immiscibility on the volatile record (S in particular) in apatite and melt inclusions are investigated. Based on our observations and fractional crystallization modeling, an explanation for high S contents in lunar apatite is presented. Last but not the least, implications for estimating the volatile budget in parental melt and lunar mantle are discussed.

2. Sample description and methods

2.1. Sample description

The CE5 sample (CE5C0800YJYX013GP) acquired for this study contains two basaltic clasts set in a one-inch epoxy mount. Clast 1 has a triangular outline with ~ 1.8 mm for the longest dimension and ~ 1 mm for the shortest dimension. Clast 2 has a rectangular outline and is ~ 2 × 1.8 mm in size (Wang et al., 2023). The mineral modal proportions of clast 1 are estimated to be 65.6 % clinopyroxene, 20.5 % plagioclase, 10.2 % ilmenite and 3.1 % Si-rich phases, while clast 2 is composed of 24.8 % clinopyroxene, 24.2 % olivine, 44.0 % plagioclase, 4.6 % ilmenite and 2.7 % Si-rich phases (Wang et al., 2023). Both clasts are coarse-grained with predominant minerals grains ~ 0.5–1 mm in length, overall exhibiting a subophitic texture. As demonstrated by the absence of olivine, clast 1 has a more evolved composition with an estimated bulk MgO content of 4.58 ± 2.59 wt% and Mg# of 25, in comparison to a bulk MgO content of 7.28 ± 2.81 wt% and Mg# of 37 for clast 2 (Wang et al., 2023).

Clinopyroxene occurs as anhedral grains (~500 μm in length), strongly zoned from Mg-rich augite cores ($Wo_{31-42}En_{29-37}Fs_{27-34}$) to Fe-rich pigeonite rims ($Wo_{8-34}En_{1-30}Fs_{41-90}$). Olivine grains are larger (~1 mm in length), also zoned with Mg-rich cores (Fo_{53-54}) and Fe-rich rims (Fo_{5-15}). Plagioclase occurs as 200 μm × 1000 μm euhedral to subhedral laths, with relatively Ca-rich cores (An_{85-87} Ab_{11-13} $Or_{0.4-0.6}$) and increased Na and K contents in the rims (An_{78-81} Ab_{16-19} Or_{1-2}) (Wang et al., 2023). Ilmenite occurs as euhedral elongated laths (~200–300 μm in length and ~ 20 μm in width) with homogenous compositions. Mesostasis assemblages include silica, felsic melt, fayalite, hyalophane, troilite, apatite, merrillite, and Zr-bearing phases (Fig. 1). These assemblages comprise incompatible-element-rich residual pockets enclosed within the framework of major minerals. Apatite is located in the mesostasis regions of the sample, which will be the focus of this study.

Apart from felsic melt in the mesostasis, felsic melt inclusions are found in the rims of plagioclase in clast 1 and olivine grains in clast 2.

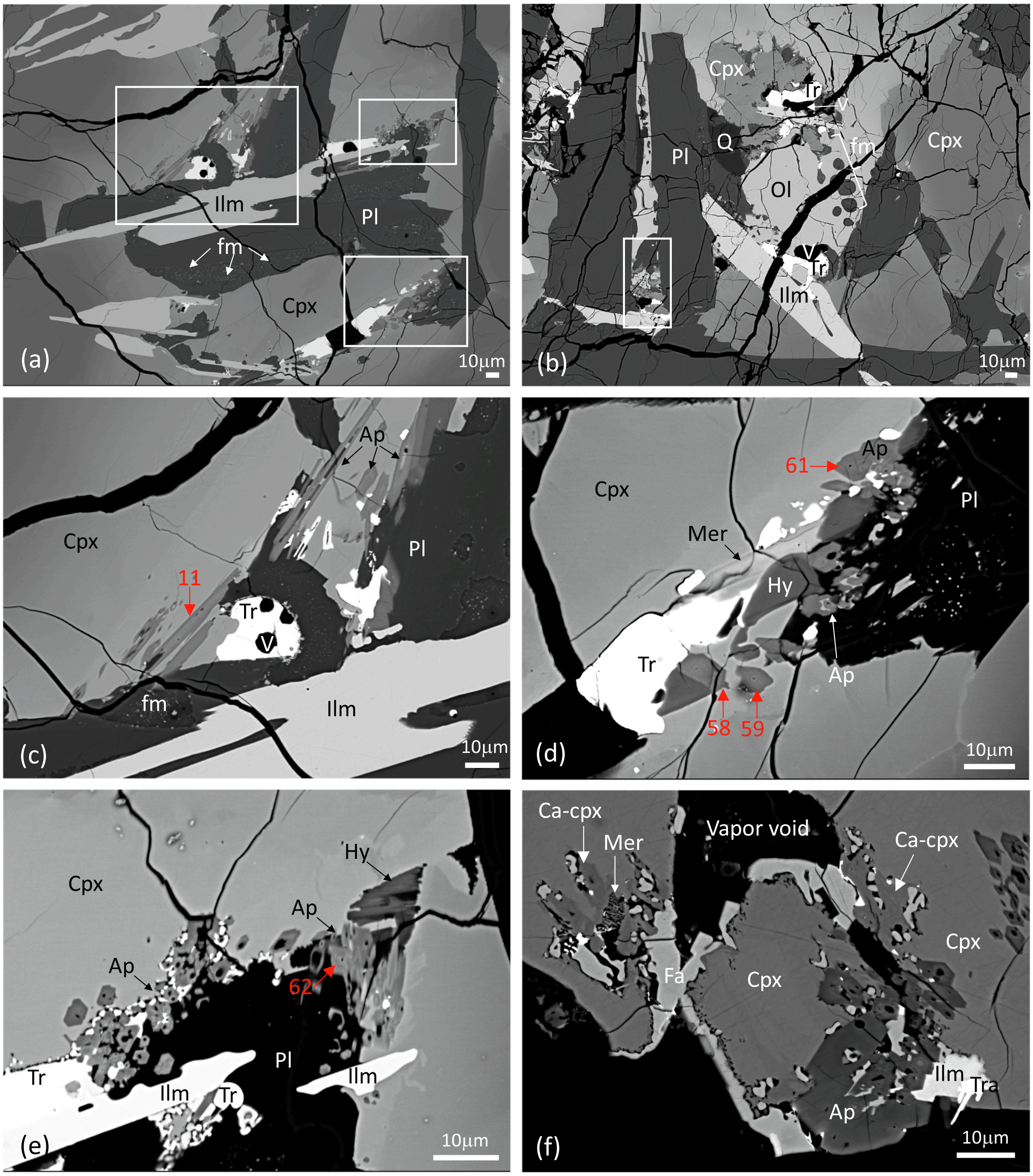

Fig. 1. Representative BSE images of the mesostasis regions in clast 1 and clast 2. (a) Mesostasis regions in clast 1 are located in the Fe-rich portions of large clinopyroxene grains. Enlarged areas shown in (c, d, e) are outlined with rectangles. (b) Mesostasis regions near the Fe-rich portion of the large olivine grains in clast 2, are comprised of clinopyroxene, ilmenite, sulfide, felsic melt, vapor voids and foam-textured phosphate. X-ray maps of the outlined area are shown in Fig. 2. (c) Elongated apatite grains containing felsic melt inclusions and possibly mafic minerals coexist with plagioclase, felsic melt and sulfide. Note the circular vapor voids in the sulfide grain. (d) Apatite grains coexist with plagioclase, merrillite, hyalophane and sulfide. (e) On the left, a cluster of tiny apatite grains with patchy zoning intergrow with a mafic mineral (possibly olivine), in close association with sulfide, ilmenite and plagioclase. On the right, the cluster of skeletal apatite grains are seen together with a group of hyalophane crystals. (f) An area showing the coexistence of fayalitic olivine, Ca, Fe-rich clinopyroxene and foam-textured merrillite. Both large euhedral apatite grains and medium-sized grains with bright cores are also observed in the same region. Phase abbreviations: Ap, apatite; Ca-cpx, Ca, Fe-rich clinopyroxene; Cpx, clinopyroxene; Fa, fayalitic olivine; Hy, hyalophane; Ilm, ilmenite; Mer, merrillite; Ol, olivine; Pl, plagioclase; Q, quartz; Tr, troilite; Tra, tranquillityite; fm, felsic melt; V, vapor void. Number labels are corresponding to the numbering for the analytical points of apatite.

Moreover, devitrified mafic inclusions are found in the core of olivine grains from clast 2. Immiscible melts are preserved in an olivine grain and an elongated ilmenite lath in clast 2. Compositional details of these melt inclusions will be presented in section 3.3.

2.2. Analytical Methods

Phase compositions were obtained using an electron microprobe (JEOL JXA 8230) at the Chinese Academy of Geological Sciences (CAGS), employing beam conditions of 15 kV and 20nA. Standards were a mix of both natural and synthetic minerals and oxides, and the quality of analyses was assessed based on stoichiometric constraints.

Apart from the common major elements, the analytical routine for melt also contained F, Cl, Ba and P; although F was shown to be always below the detection limit of ~ 30 ppm. The detection limits for Cl, Ba and P are approximately 20, 80 and 100 ppm, respectively. For the analysis of apatite, additional elements of Sr, La, Ce and Y were also analyzed, with detection limits of ~ 150, ~300, ~1000 and ~ 300 ppm, respectively. Strontium sulfate SrSO4, phosphates LaP_5O_{10}, CeP_5O_{10} and yttrium vanadate YVO_4 were the calibrating standards for Sr, La, Ce and Y, respectively. Durango apatite has been used as the standard for F, Ca and P with recommended values from Young et al. (1969); Cl was standardized using NaCl. Fluorine was always analyzed in the first pass, with 20 s counting time utilizing LDE1 analyzing crystal resulting in a detection limit of ~ 200 ppm. For reduced lunar conditions, S should be present in its reduced form as S^{2-}; therefore, ZnS was used as the calibrating standard for S. With a PETH crystal and 50 s counting time (background always counted for half the peak time), the detection limit for S is ~ 50 ppm in melt and ~ 60 ppm in apatite. Analyses of a secondary standard VG-2 returned an average S content of 1372 ± 52 ppm for six data points in one session.

Analyzing F in apatite has complications associated with F X-ray intensity variation due to beam bombardment (Stormer et al., 1993). Different approaches have been suggested to mitigate such a problem, e. g., select apatite crystals oriented with their c axis perpendicular to the incident beam; reduce beam current and counting time; enlarge beam diameter; and time-dependent intensity (TDI) correction of F count rate back to time-zero (McCubbin et al., 2010b; Goldoff et al., 2012). Due to the small grain size for apatite in our sample and unavailability of TDI correction on the probe we used, we were not able to implement all these measures, and F content in apatite grains oriented with c axis parallel to the incident beam may be overestimated.

X-ray elemental maps were acquired for two selected areas in the sample using five wavelength-dispersive spectrometers (WDS) simultaneously at CAGS. Elements analyzed were Ca, Ce, Cl, F, Fe, Mg, Na, P, S and Si. Acquisitions were performed with a focused beam of 20 kV and 50nA, a dwell time of 50 ms and a step size of 1 μm.

3. Results

3.1. Phase relations of the mesostasis

Apatite is found to be closely associated with clinopyroxene, ilmenite, plagioclase, troilite, olivine, hyalophane, merrillite, Zr-bearing minerals and felsic melt in the mesostasis regions of the sample; which are located in the most Fe-rich portion of the clinopyroxene grains in clast 1 (Fig. 1a) and the olivine grains of clast 2 (Fig. 1b). Representative compositions for phases in association with mesostasis can be found in the supplementary material (Table S1). Degassing is indicated by voids left by vapor bubbles of circular or irregular shape (Fig. 1a, b, c, f). They are often closely associated with felsic melt or sulfide. The irregular shapes are due to the space restriction of neighboring minerals (Fig. 1b, f). Apatite grains appear in clusters with various shapes and sizes (<1 to 5 μm), from well-defined hexagonal and columns to skeletal crystals (Fig. 1c, d, e, f). Although rare elongated grains with lengths up to 50 μm have been found (Fig. 1c), the short dimensions of these grains are normally less than 5 μm.

In clast 1, olivine is not a part of the main crystallizing assemblage. However, in one area, along the edge of an Fe-rich clinopyroxene grain, irregular-shaped fayalitic olivine grains are found coexisting with Ca, Fe-rich clinopyroxene, along with an unidentified foam-like phosphate mineral and tiny sulfide grains (Fig. 1f). The coexistence of Ca, Fe-rich clinopyroxene and fayalitic olivine is similar to that observed in the mesostasis regions of clast 2 (Fig. 1b). In order to identify this foam-textured phosphate phase, X-ray mapping of such an example from clast 2 is shown in Fig. 2. The mesostasis region of interest is enclosed between large plagioclase and ilmenite laths. Felsic melt can be identified by the high Si signal; the foam-textured phosphate is identified as merrillite by matching Ca and P signals and the absence of F and Cl. The olivine grain contains worm-like melt inclusions, below which lies an apatite grain, as confirmed by matching Ca, P, F and Cl signals. The F signals obtained from olivine and sulfide are due to peak-overlap from their high FeO contents. It is interesting to note that the clinopyroxene grain sitting in-between the two sulfide grains has higher MgO and lower CaO contents than the clinopyroxene grain above, representing an earlier stage of crystallization. The enrichment of sodium in the surrounding plagioclase grains is also shown here in the Na X-ray map (Fig. 2).

Well-crystallized merrillite has also been identified in both clasts. It appears brighter than apatite in back-scattered electron (BSE) images, similar to that of clinopyroxene (Fig. 1d). Detecting and distinguishing merrillite from clinopyroxene presents difficulties. In closeup, merrillite has a lower relief than clinopyroxene (Fig. 1d; Fig. 3). X-ray mapping of an area of coexisting apatite, merrillite and clinopyroxene from clast 1 is shown in Fig. 3. Merrillite and apatite can be distinguished by lower CaO, higher REEs, and the absence of F and Cl in merrillite. Uneven distribution of F and Cl in apatite is noteworthy. Trends of decreasing MgO and increasing FeO contents in clinopyroxene towards the enclosed mineral assemblage (apatite, merrillite, ilmenite, troilite and plagioclase) are shown in the Mg and Fe X-ray maps.

Spot analyses of merrillite returned nearly uniform compositions, with the average compositions reported in Table 1. Merrillites from the two clasts show similar compositions, the only difference being the higher FeO (7.19 wt% vs 5.63 wt%) and lower MgO (0.14 wt% vs 0.49 wt%) contents in merrillites from clast 1 compared to clast 2, in consistence with the bulk compositions of these two clasts.

3.2. Apatite compositions

Due to the rarity of mesostasis and the limited number of apatite analyses obtained from clast 2, apatite compositional data reported and discussed here are from clast 1. It can be seen in BSE images that apatite grains always display some level of compositional heterogeneity, even in tiny skeletal crystals (Fig. 1c, d, e, f). Moreover, bigger apatite grains may result from the “fusion” of smaller grains, their zoning patterns therefore appear to be rather complex (Fig. 4a, c). We obtained the data for a total of 45 analytical points. Due to the small grain size and complex zoning, apatite analyses often show some level of contamination from neighboring minerals or inclusions. Data chosen for further discussion and graph plotting (totaling 35 data points) show good stoichiometry (Tables 2-4, Table S2), the only exception being data for medium-sized euhedral apatite grains with bright cores (Fig. 4c). It is a formidable task to obtain analyses from the core, mantle and rim of these small zoned apatite grains. Some data points used in the graph plotting have cation sums for both P and Ca sites showing deviations of up to 0.1–0.2 from the ideal values (Table 4). As the contamination from clinopyroxene or felsic melt inclusion only has a dilutional effect on REEs and volatile contents, data points with clear contamination are also shown in Table 4 for the convenience of discussing the zoning pattern.

We were able to identify three different zoning profiles, represented by a large euhedral apatite grain with fractional crystallization (FC)-dominated zoning (Fig. 4a, Table 2), an elongated apatite grain with

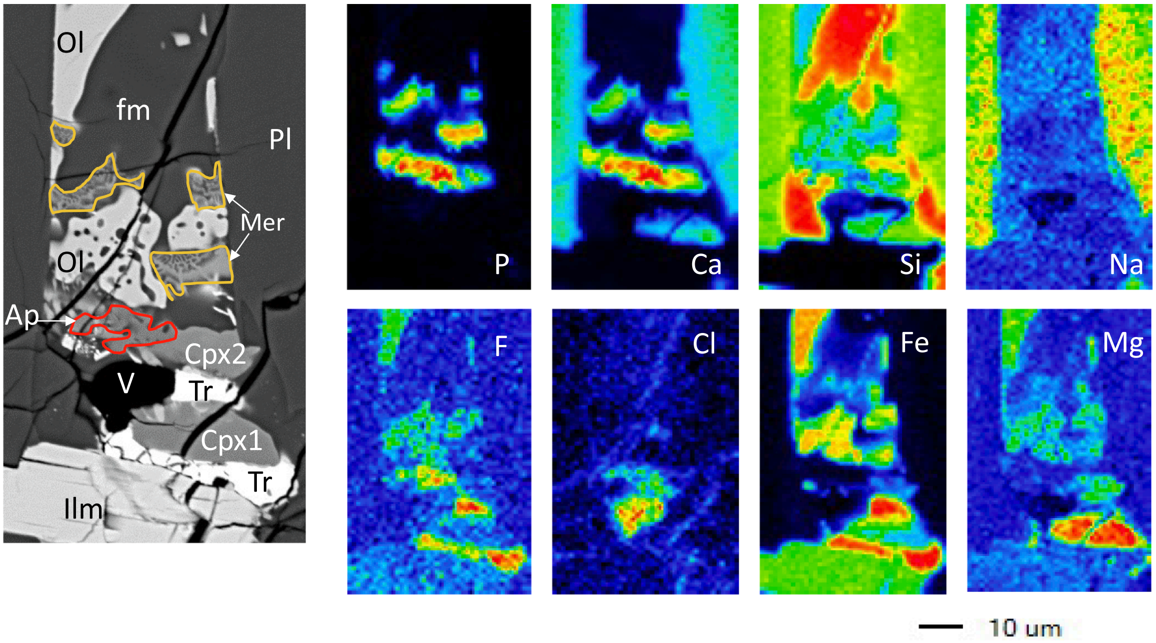

Fig. 2. X-ray mapping of a mesostasis region from clast 2, showing the phase assemblage of Fe-rich olivine, clinopyroxene, apatite, foam-textured merrillite, troilite, felsic melt and vapor void. The scale bar is for the X-ray maps only. The BSE image is enlarged to show more details. Merrillite and apatite are outlined in the BSE image using orange and red colors respectively. F signals shown for Fe-rich olivine and troilite are due to peak-overlap from their high FeO contents. The high Cl signal for the vapor void is from the epoxy. Phase abbreviations are as in Fig. 1.

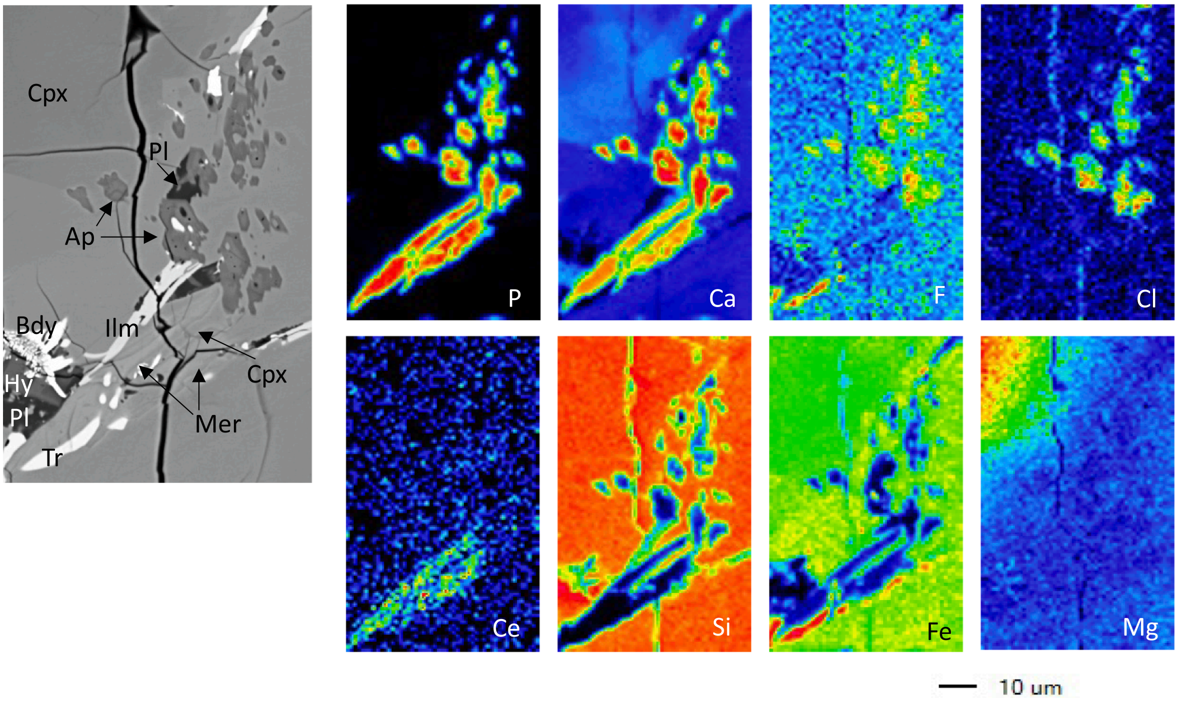

Fig. 3. X-ray mapping of a mesostasis region from clast 1, showing the phase assemblage of Fe-rich clinopyroxene, apatite, merrillite, troilite and ilmenite. The scale bar is for the X-ray maps only. The BSE image is enlarged to show more details. Phase abbreviations are as in Fig. 1, with the addition of "Bdy" for baddeleyite.

degassing-induced zoning (Fig. 4b, Table 3) and medium-sized euhedral apatite grains with bright cores (Fig. 4c, Table 4). The remaining data points (e.g., Fig. 4d, Table S2) are grouped as "individual analyses" for the ease of discussion and graph plotting. For the FC-dominated zoning (Fig. 4a), F decreases from core to rim, while other elements such as Cl, S, REEs, SrO, TiO_2, FeO and SiO_2 increase (Fig. 5). The identification of degassing-induced zoning in the elongated apatite grain is based on its increasing F content, and decreasing Cl and S contents from core to rim (Fig. 5). We remain intrigued by the fact that both volatiles and nonvolatile elements in the degassing profile show opposite trends to those observed in the FC-dominated zoning profile (Fig. 5), possible explanations will be discussed in section 4.3. It is noteworthy that the concentrations of Cl, S, FeO, SiO_2 and TiO_2 are higher in the degassing profile than those in the FC-dominated zoning profile (Fig. 5 and

Table 1
Average merrillite compositions from both clasts.

Sample	Mer-clast 1	σ(5)	Mer-clast 2	σ(2)
P_2O_5	41.63	*0.41*	42.65	*1.12*
SiO_2	0.81	*0.32*	0.44	*0.00*
TiO_2	0.25	*0.27*	0.14	*0.11*
Al_2O_3	0.13	*0.11*	0.03	*0.01*
FeO	7.19	*0.38*	5.63	*0.12*
MnO	0.07	*0.03*	0.10	*0.03*
MgO	0.14	*0.11*	0.49	*0.11*
CaO	39.55	*0.40*	41.21	*1.14*
Na_2O			0.016	*0.004*
K_2O	0.09	*0.11*	0.061	*0.004*
SrO	0.30	*0.03*	0.26	*0.03*
La_2O_3	1.34	*0.22*	1.14	*0.09*
Ce_2O_3	3.85	*0.41*	3.32	*0.42*
Y_2O_3	2.08	*0.36*	1.71	*0.18*
F			0.02	*0.03*
Cl	0.005	*0.003*	0.005	*0.004*
S(ppm)	416	*265*	22	*20*
O=F+Cl + S	0.02	*0.01*	0.02	*0.02*
Total	97.46	*0.54*	97.22	*1.63*
Structure formula based on 56 oxygens				
P	13.730	*0.099*	13.934	*0.056*
Si	0.318	*0.123*	0.169	*0.002*
Ti	0.072	*0.080*	0.040	*0.031*
Sum P site	14.119	*0.110*	14.142	*0.085*
Al	0.059	*0.050*	0.013	*0.004*
Fe	2.343	*0.122*	1.818	*0.002*
Mn	0.025	*0.008*	0.033	*0.010*
Mg	0.082	*0.065*	0.285	*0.070*
Ca	16.509	*0.112*	17.036	*0.095*
Na			0.012	*0.003*
K	0.043	*0.056*	0.030	*0.003*
Sr	0.067	*0.006*	0.059	*0.008*
La	0.193	*0.032*	0.163	*0.016*
Ce	0.550	*0.060*	0.470	*0.070*
Y	0.432	*0.075*	0.352	*0.044*
Sum others	20.302	*0.184*	20.270	*0.130*
F			0.024	*0.034*
Cl	0.003	*0.002*	0.003	*0.003*
S	0.030	*0.019*	0.002	*0.001*

compare Table 2 and 3). Medium-sized euhedral apatite grains often display zoning with brighter cores (Fig. 4a, c), corresponding to higher REE contents. While F, SiO_2, and FeO are generally higher in the core, Cl and S contents are higher in the rim (Fig. 4c and Table 4).

The Ce_2O_3 versus Cl plot is used to showcase the variation of apatite compositions (Fig. 6a). Two distinctive groups can be identified. One group is characterized with a large range of Cl contents (~0.3–1.1 wt%) and a medium level of REE concentrations (~0.3–0.6 wt% for Ce_2O_3). These data points represent the FC-dominated zoning and the degassing-induced zoning profiles. The other group is characterized with a large range of REE contents (~0.3–1.3 wt% for Ce_2O_3) and comparatively lower Cl contents (~0.2–0.6 wt%). These data points represent medium-sized apatite grains with bright cores, and hence show a negative correlation between Cl and REEs. Individual analyses of apatite grains, fall mostly within the trend defined by the medium-sized euhedral grains with bright cores. One single analysis (apatite No.62, Table S2) from the skeletal apatite cluster (Fig. 1e) shows an enrichment in REEs (0.97 wt% for Ce_2O_3) and relative depletion in Cl (0.24 wt%) and S (666 ppm), similar to the bright cores of euhedral apatite grains. Similarly, some elongated grains with bright cores also returned high REE contents (e.g., 1.02 wt% of Ce_2O_3 in apatite No.8 in Fig. 4d, Table S2). The difference is that the elongated grains have the highest F contents (e.g., 3.83 wt% of F in apatite No.8, exceeding that for pure fluorapatite).

S contents in apatite also vary in a large range. The positive correlation between Cl and S is a prominent feature (Fig. 6b). There are three data points lying above the main trend of correlation as shown in Fig. 6b. Considering that they are all analyses near sulfide, we cannot rule out that these high values are analytical artifacts. For the remaining data points following the main trend, S contents vary in the range ~ 130 to ~ 3000 ppm, with values higher than 2000 ppm only belonging to the apatite grain with degassing-induced zoning. For the apatite grain with FC-dominated zoning, S content increases ten times from ~ 150 ppm in the core to ~ 1700 ppm in the rim.

Apatite compositions reported here show relatively low F and high Cl characteristics, with the majority data points having F contents in the range 0.97–2.47 wt%, and Cl contents in the range 0.24–1.09 wt%. In the ternary plot of Cl + S-OH-F endmembers for apatite (Fig. 7), the data points lie away from the Cl + S apex, and span a large range along the F-OH binary edge. There is a lack of F-rich apatite compositions from our sample, with most compositions forming a cluster in the mid-section between the F and OH apexes, showcasing that estimated mole fractions for the OH-Ap endmember (~0.10–0.67) varying in a similar range to that for the F-Ap endmember (~0.26–0.80). There are only two data points lying outside this range, with F contents of 2.93 and 3.83 wt%, respectively; the latter is not shown in Fig. 7 as its F content exceeds that for pure fluorapatite. These apatite compositions are distinct from previously reported apatite compositions for Apollo high-Ti and low-Ti mare basalts (McCubbin et al., 2023), but show similarities to the apatite compositions from meteorites LAP 04841 and MIL 05035 (Fig. 7). For example, Tartèse et al. (2013) reported F and Cl contents of 0.73–1.73 wt% and 0.14–0.76 wt% for apatites from LAP 04841; and apatites from MIL 05035 have been shown to have 1.43–1.90 wt% F and 0.58–1.13 wt% Cl (Joy et al., 2008).

Ji et al. (2022) reported apatite compositions obtained from a set of 23 smaller CE5 basaltic clasts based on NanoSIMS analyses, which span large ranges of 0.91–3.93 wt% F, 820–11989 ppm Cl and 134–6564 ppm H_2O. Although apatite compositions from clast 1 fall in the large range reported by Ji et al. (2022), there are only a few data points overlapping with those reported by Ji et al. (2022) in the ternary plot of Fig. 7. The disparity may result from an overestimation of OH mole fraction in apatite from clast 1 and an overestimation of F mole fraction in apatite for data from Ji et al. (2022).There have been reports that H_2O contents in apatite calculated based on F and Cl contents are higher than NanoSIMS analyses (Barrett et al., 2023; Martínez et al., 2023). The underlying cause is the presence of vacancies and other anions or molecules in the apatite anion column (Pan and Fleet, 2002). This will lead to an overestimation of OH in apatite when assuming F+Cl + OH=1. Moreover, the sums of calculated F, Cl and OH mole fractions for the analyses reported by Ji et al. (2022) vary between 0.35 and 1.2, with an average value of 0.75. When plotted in Fig. 7, the sums of their F, Cl and OH mole fractions have been normalized to 1. In the case of the sum of F, Cl and OH mole fractions much under unity, normalization to 1 will lead to the largest overestimation for the F mole fraction in apatite, as F is the dominant volatile. It appears to be a similar case for MIL 05035, with the electron probe microanalyses (EPMA) from Tartèse et al. (2013) and NanoSIMS analyses from Wang et al. (2019) displaying a similar disparity as shown in Fig. 7. As OH in apatite is calculated as OH=1-F-Cl for the EPMA data and F in apatite is calculated as F=1-Cl-OH for NanoSIMS data, the disparity between the two suggests that the sums of F, Cl and OH mole fractions are under unity, supporting the presence of vacancies and other anions in the apatite anion column.

3.3. Record of melt immiscibility and compositions

The felsic melts in clast 1 have high SiO_2 (80.06 ± 1.68 wt%), Al_2O_3 (10.15 ± 0.64 wt%) and K_2O (3.60 ± 0.63 wt%), low CaO (1.00 ± 0.19 wt%), FeO (2.44 ± 0.80 wt%) and negligible MgO (0.014 ± 0.013 wt%) contents. Despite the simplicity in composition, systematic variations have been observed, with positive correlations between Al_2O_3, BaO and P_2O_5 being the most prominent (Fig. 8a, b). In particular, felsic melt patches contained in the rim of large plagioclase grains appear to have lower Al_2O_3, BaO and P_2O_5 contents in comparison to felsic melts in the mesostasis (Fig. 8a, b). Sub-micron bright spheres are commonly seen in the felsic melt patches contained in plagioclase (Fig. 1a; 8c), but are

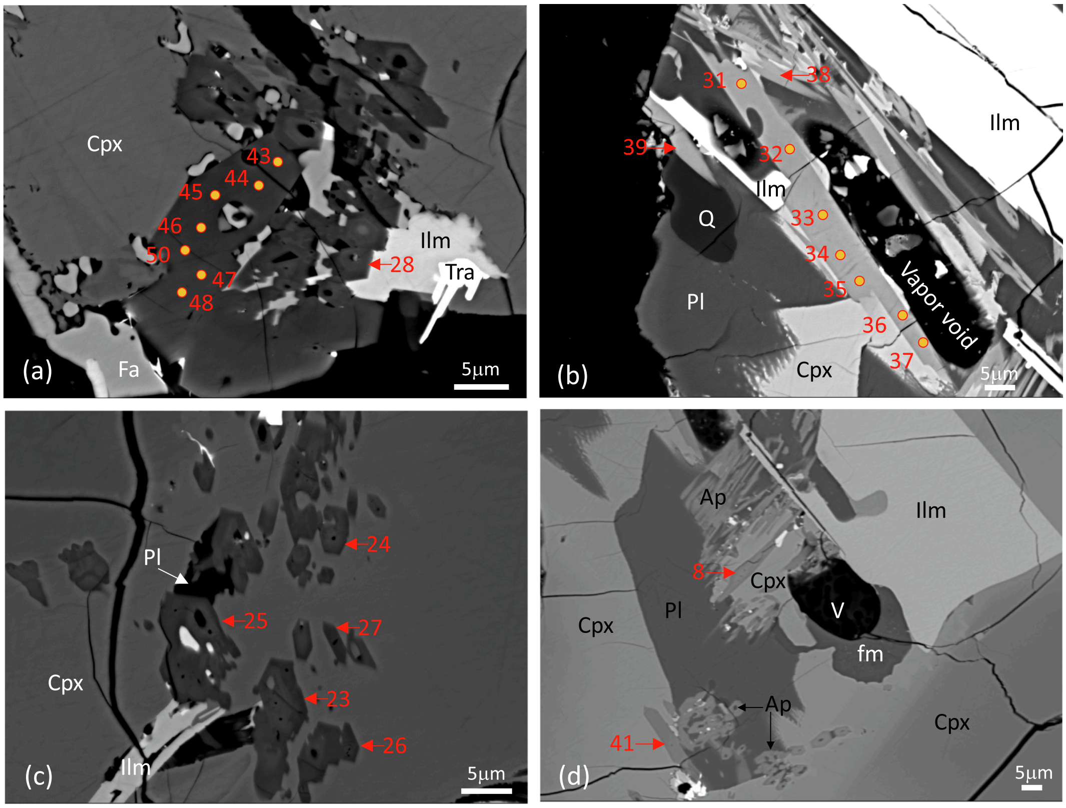

Fig. 4. BSE images for representative apatite compositional groups. (a) A large euhedral apatite grain, from which a fractional crystallization-dominated zoning profile was obtained with analytical points of 43–46 and 50. (b) An elongated apatite grain near a large vapor void, from which a degassing-induced zoning profile was obtained with analytical points of 31–37. (c) The cluster of apatite grains with bright cores, from the same area as shown in Fig. 3. (d) In the area below the elongated apatite grain shown in (b), two clusters of apatite display different compositional characters, with the cluster above showing bright cores due to high REE contents, and the cluster below similar to the rim of the degassing profile in (b). Phase abbreviations are as in Fig. 1. Number labels are corresponding to the numbering for the analytical points.

generally absent in the felsic melts of mesostasis. Due to the minute size of the bright spheres, their precise compositions cannot be determined. Nevertheless, based on the negative correlation between SiO_2 and FeO contents for felsic melts in plagioclase (Fig. 8d), we interpretate that the bright spheres most likely represent the immiscible mafic melt trapped in the felsic melt patch after immiscibility occurred. Most of these felsic melts have S contents less than 100 ppm, however, higher values up to 356 ppm have been obtained, which may be due to contamination from the bright spheres.

Evidence of melt immiscibility is well preserved in clast 2. A pair of mafic and felsic melt patches are found in contact with grains of sulfide and plagioclase, hosted within a larger olivine grain (Fig. 9a). A few devitrified melt inclusions are found in large olivine grains, which are characterized by barred and skeletal aggregates (<5 μm) of near-stoichiometric pyroxene set in the interstitial glass matrix (Fig. 9b). An elongated melt inclusion (~500 μm long and ~ 10 μm wide) in a large ilmenite lath preserved two immiscible melts with the felsic melt appearing as spherules of 1–3 μm in diameter floating in the mafic melt (Fig. 9c). Mesostasis regions are rare in clast 2; and the most prominent feature is the felsic melt inclusions contained in the Fe-rich portions of the large olivine grains (Fig. 9d).

Based on the MgO contents of the melt inclusions in clast 2 (Fig. 10; Table 5), it can be inferred that the immiscible melt pair in olivine represent an earlier stage of melt with 6 wt% MgO in the immiscible mafic melt; the devitrified melt inclusions may be slightly later with 2.5 wt% MgO; while the elongated melt inclusion in ilmenite is the latest with 0.6 wt% MgO in the immiscible mafic melt. The devitrified melt inclusions have higher TiO_2 and P_2O_5 contents than the immiscible melt inclusions (Fig. 10), suggestive of entrapment before ilmenite and phosphate crystallization. The low Al_2O_3 contents of the early-stage immiscible felsic melts are noteworthy, 5.48 wt% and 6.74 ± 0.22 wt % for felsic melts in olivine and ilmenite, respectively. The late-stage immiscible felsic melts, preserved as olivine inclusions or in the mesostasis, are characterized with the highest K_2O (4.92 ± 0.94 wt%) and BaO (0.77 ± 0.32 wt%) contents (Fig. 10, Table 5). Note that the relatively large standard deviations for the average compositions of late-stage felsic melts reflect compositional variation similar to that observed for the felsic melts of clast 1.

Defocused beam analyses of devitrified melt inclusions in olivine indicate that the original melt prior to devitrification contained ~ 1500 ppm S. The well-preserved melt pair next to a troilite grain in olivine have ~ 2600 and ~ 500 ppm S in the mafic and felsic melts, respectively. Similarly, the immiscible felsic melts preserved in ilmenite have on average ~ 500 ppm S, while the mafic melts contain on average ~ 2500 ppm S. Sulfur contents in the late-stage felsic melts are generally less than 100 ppm (Fig. 10, Table 5).

4. Discussion

4.1. Melt immiscibility, sulfide saturation and degassing

The different episodes of melt immiscibility observed in clast 2 suggest that melt immiscibility is not limited to the late stages of melt evolution and may occur throughout the evolutionary process. Apollo sample 12032,366–18 is a Th-rich evolved basalt with 4.2 wt% TiO_2, 11.7 wt% Al_2O_3, and 0.25 wt% K_2O, similar to the bulk compositions of clast 2. An experimental study of the crystallization process of Apollo sample 12032,366–18 by Stadermann et al. (2022) has bracketed the

Table 2
Apatite compositions along the fractional crystallization zoning profile shown in Fig. 4a.

Analytical No.	CE5-1-AP-43	CE5-1-AP-44	CE5-1-AP-45	CE5-1-AP-46	CE5-1-AP-50[a]
P_2O_5	39.73	40.54	40.21	40.98	37.79
SiO_2	1.46	0.96	0.72	0.93	*6.44*[a]
TiO_2	0.066	0.039	0.029	0.002	0.135
Al_2O_3	0.036	0.007	0.008		0.213
FeO	2.17	1.97	1.70	1.86	*5.28*[a]
MnO	0.03		0.08	0.03	0.05
MgO		0.012			0.008
CaO	53.19	54.16	55.07	54.35	49.57
K_2O	0.010	0.014	0.007	0.010	0.063
SrO	0.27	0.21	0.19	0.20	0.22
La_2O_3	0.09	0.04	0.04	0.03	0.14
Ce_2O_3	0.52	0.40	0.46	0.39	0.52
Y_2O_3	0.25	0.17	0.30	0.23	0.34
F	1.50	1.71	2.18	2.24	1.70
Cl	0.75	0.66	0.28	0.56	0.60
S(ppm)	1704	767	147	367	1162
O=F+Cl + S	1.68	1.78	1.97	2.16	1.76
Total	98.55	99.18	99.31	99.69	101.43
Structure formula based on 12.5 oxygens					
P	2.866	2.899	2.881	2.911	2.634
Si	0.124	0.081	0.061	0.078	0.530
Ti	0.004	0.002	0.002		0.008
sum P site	5.061	5.076	5.158	5.053	*4.813*[a]
Al	0.004	0.001	0.001		0.021
Fe	0.155	0.139	0.120	0.131	0.364
Mn	0.002		0.006	0.002	0.004
Mg		0.002			0.001
Ca	4.856	4.902	4.992	4.886	4.372
K	0.001	0.002	0.001	0.001	0.007
Sr	0.013	0.010	0.009	0.010	0.011
La	0.003	0.001	0.001	0.001	0.004
Ce	0.016	0.012	0.014	0.012	0.016
Y	0.011	0.007	0.013	0.010	0.015
sum Ca site	2.995	2.982	2.944	2.990	*3.173*[a]
F	0.404	0.457	0.585	0.596	0.442
Cl	0.108	0.095	0.040	0.079	0.083
S	0.027	0.012	0.002	0.006	0.018
[b]OH cal	0.461	0.436	0.373	0.320	0.457
H_2O cal(wt %)	0.825	0.781	0.669	0.572	0.818
[c]X_F	0.398	0.454	0.580	0.596	0.451
[c]X_{Cl}	0.110	0.098	0.041	0.082	0.088

[a] This data point (No. 50) is contaminated with clinopyroxene, as shown by the high SiO_2 and FeO contents (italicized) and anomalous total cation numbers for both Ca site and P site(italicized), but shown here for the completeness of the profile.

[b] Mole fraction of OH endmember is calculated assuming F+Cl + S+OH=1.

[c] Mole fractions of F and Cl in apatite are calculated following Piccoli and Candela (2002) with equations of $X_F = C_F/3.767$ and $X_{Cl} = C_{Cl}/6.809$, where X_F and X_{Cl} are mole fractions of F and Cl in apatite and C_F and C_{Cl} are F and Cl contents in apatite in wt%.

Table 3
Apatite compositions along the degassing zoning profile shown in Fig. 4b.

Analytical No.	CE5-1-AP-31	CE5-1-AP-32	CE5-1-AP-33	CE5-1-AP-34	CE5-1-AP-35	CE5-1-AP-36	CE5-1-AP-37
P_2O_5	38.69	39.53	38.44	38.08	39.02	39.38	39.08
SiO_2	2.29	1.68	2.17	2.34	2.04	1.75	1.80
TiO_2	0.18	0.18	0.22	0.19	0.21	0.15	0.16
Al_2O_3	0.07	0.05	0.07	0.07	0.07	0.04	0.12
FeO	2.88	2.62	3.16	3.62	3.26	2.95	3.20
MnO	0.11	0.06	0.14	0.12	0.08	0.09	0.08
MgO	0.030		0.008				0.001
CaO	52.21	52.64	51.19	51.15	50.90	51.62	51.80
K_2O	0.042	0.017	0.011	0.019	0.005	0.016	0.014
SrO	0.14	0.25	0.26	0.22	0.24	0.22	0.21
La_2O_3	0.02	0.13	0.13	0.13	0.09	0.14	0.09
Ce_2O_3	0.33	0.41	0.47	0.61	0.42	0.40	0.47
Y_2O_3	0.31	0.25	0.16	0.14	0.23	0.22	0.19
F	2.01	2.18	1.65	1.41	1.61	1.53	1.63
Cl	0.64	0.78	1.05	1.09	1.07	0.97	0.83
S(ppm)	722	1405	2420	2635	3052	2431	2302
O=F+Cl + S	2.01	2.26	1.99	1.81	1.99	1.85	1.86
Total	97.99	98.65	97.38	97.66	97.55	97.87	98.03
Structure formula based on 12.5 oxygens							
P	2.807	2.853	2.817	2.793	2.847	2.862	2.841
Si	0.196	0.143	0.188	0.203	0.176	0.150	0.155
Ti	0.011	0.012	0.014	0.013	0.013	0.010	0.010
sum P site	5.054	5.044	5.036	5.069	4.987	5.010	5.051
Al	0.007	0.005	0.008	0.007	0.007	0.004	0.012
Fe	0.206	0.186	0.229	0.262	0.235	0.212	0.230
Mn	0.008	0.005	0.010	0.009	0.006	0.006	0.006
Mg	0.004		0.001				
Ca	4.793	4.806	4.748	4.747	4.700	4.748	4.765
K	0.005	0.002	0.001	0.002	0.001	0.002	0.002
Sr	0.007	0.012	0.013	0.011	0.012	0.011	0.011
La	0.001	0.004	0.004	0.004	0.003	0.005	0.003
Ce	0.010	0.013	0.015	0.019	0.013	0.012	0.015
Y	0.014	0.011	0.008	0.007	0.010	0.010	0.009
sum Ca site	3.014	3.007	3.020	3.008	3.036	3.022	3.005
F	0.543	0.588	0.452	0.385	0.440	0.415	0.442
Cl	0.093	0.113	0.154	0.160	0.156	0.142	0.120
S	0.012	0.022	0.039	0.043	0.049	0.039	0.037
[b]OH cal	0.352	0.277	0.355	0.412	0.355	0.405	0.401
H_2O cal(wt %)	0.631	0.495	0.635	0.737	0.635	0.725	0.718
[c]X_F	0.532	0.579	0.439	0.373	0.429	0.405	0.432
[c]X_{Cl}	0.094	0.115	0.154	0.160	0.157	0.143	0.121

Footnotes are the same as for Table 2.

onset of liquid immiscibility between 1024 and 1002 °C. Their experimental results have shown a relative enrichment of Ti, Fe, Mn, Mg, Ca, Ba, P and Zr in the immiscible mafic melt, while Si, Al, Na and K are preferred by the felsic melt. Similar observations have been made for the immiscible melt pairs found in both olivine and ilmenite from clast 2 (Fig. 11), with partition coefficients obtained from the melt pair in ilmenite being closer to the experimental values from Stadermann et al. (2022), indicative of a similar stage of evolution. The higher partition coefficients of Fe, Mn, Mg and Ca for the melt pair in olivine, are a unique feature which can be explained by the low concentrations of these elements in the felsic melt. The relative enrichments of Al_2O_3 in mafic melt and BaO in felsic melt are different from the experimental observations of Stadermann et al. (2022). However, the uncertainty is large for partition coefficients with values close to ~ 1.

Moreover, Stadermann et al. (2022) have shown that, with decreasing temperature, this is a further divergence between the immiscible mafic and felsic melt compositions, that is, Fe, Mg, Mn, Ca, Ti and P will concentrate further in the mafic melt, while Si, Al, Na, K and Ba will partition more into the felsic melt. Previous studies of natural samples and experiments have also shown that partition coefficients for BaO between mafic and felsic melts change from > 1 to < 1 as the immiscibility gap becomes wider (Shearer et al., 2001). The increasing Al, Na, K and Ba contents from the felsic melt in olivine, to the felsic melt in ilmenite, and then to the late-stage felsic melts, are in agreement with such a prediction (Fig. 10). Immiscible melt inclusions found in Apollo samples (compiled by Zeng et al. (2020)) are also shown in Fig. 10 for comparison. The immiscible felsic melt inclusions have major element compositions similar to the late-stage felsic melts from our sample; while the corresponding immiscible mafic melt inclusions show lower SiO_2, Al_2O_3 and CaO, higher FeO, TiO_2 and P_2O_5 contents compared to the early-stage immiscible mafic melts observed in our sample; indicating that they also record a late-stage melt immiscibility.

After melt immiscibility, the relative enrichment of mafic components and depletion of felsic components in the immiscible mafic melt kick-started the crystallization sequence again. The rim of clinopyroxene grains, approaching ferrosilite in composition, crystallized from the immiscible mafic melt, has lower Mg#, CaO, Al_2O_3, and TiO_2 contents compared to the core composition (Wang et al., 2023). This reflects the trend of melt compositional evolution due to fractional crystallization

Table 4
Compositions for medium-sized euhedral apatite grains with bright cores.

Analytical No.	CE5-ap23 −core	CE5-ap23 −mantle	CE5-ap23 −rim[a]	CE5-ap24 −core	CE5-ap25 −core[a]	CE5-ap25 −mantle1	CE5-ap25 −mantle2	CE5-ap26 −rim	CE5-ap27 −rim[a]	CE5-ap28 −core[a]	CE5-ap28 −rim
P_2O_5	35.99	38.37	29.06	35.97	31.92	37.38	38.61	36.34	31.99	36.83	38.01
SiO_2	6.81	4.25	17.34	3.81	10.18	5.36	2.05	3.14	13.95	9.59	2.93
TiO_2	0.20	0.13	0.33	0.58	0.19	0.25	0.20	0.07	0.30	0.08	0.06
Al_2O_3	0.82	0.03	0.36	0.06	1.09	0.51	0.08	0.05	0.27	0.64	0.17
FeO	5.41	3.22	16.67	3.81	3.34	5.12	3.35	3.02	12.10	2.48	2.12
MnO	0.09	0.13	0.19	0.04	0.04	0.10	0.06	0.14	0.15	0.10	0.02
MgO	0.007	0.025	0.037			0.079	0.006		0.005		0.036
CaO	48.14	50.97	40.67	49.78	44.83	48.96	53.46	53.50	43.92	49.96	54.08
K_2O	0.197	0.015		0.006	0.481	0.014	0.024	0.004		0.455	0.055
SrO	0.21	0.25	0.22	0.25	0.16	0.26	0.22	0.26	0.16	0.21	0.28
La_2O_3	0.35	0.39	0.05	0.28	0.33	0.22	0.18	0.13		0.29	0.19
Ce_2O_3	1.10	1.30	0.24	1.08	1.26	0.61	0.62	0.37	0.27	0.92	0.74
Y_2O_3	0.85	0.91	0.09	0.71	0.66	0.23	0.25	0.23	0.10	0.71	0.25
F	1.99	2.04	0.72	1.35	1.40	1.20	1.30	1.31	1.29	1.81	0.97
Cl	0.25	0.24	0.36	0.32	0.18	0.35	0.55	0.42	0.41	0.17	0.46
S(ppm)	200	188	776	288	804	2444	2564	268	288	164	468
O=F+Cl + S	1.80	1.83	0.81	1.30	1.30	1.29	1.47	1.31	1.29	1.61	1.05
Total	100.64	100.44	105.62	96.77	94.84	99.59	99.75	97.72	103.66	102.65	99.37
	Structure formula based on 12.5 oxygens										
P	2.548	2.721		2.667		2.658	2.776	2.671			2.729
Si	0.569	0.356		0.334		0.450	0.174	0.273			0.249
Ti	0.013	0.008		0.038		0.016	0.013	0.005			0.004
sum P site	4.894	4.922		5.048		4.881	5.165	5.251			5.147
Al	0.081	0.003		0.006		0.050	0.008	0.005			0.017
Fe	0.378	0.225		0.279		0.359	0.238	0.219			0.150
Mn	0.006	0.009		0.003		0.007	0.005	0.010			0.002
Mg	0.001	0.003				0.010	0.001				0.005
Ca	4.314	4.575		4.670		4.405	4.865	4.977			4.914
K	0.021	0.002		0.001		0.001	0.003				0.006
Sr	0.010	0.012		0.012		0.013	0.011	0.013			0.014
La	0.011	0.012		0.009		0.007	0.006	0.004			0.006
Ce	0.034	0.040		0.035		0.019	0.019	0.012			0.023
Y	0.038	0.041		0.033		0.010	0.011	0.011			0.011
sum Ca site	3.130	3.085		3.039		3.124	2.963	2.949			2.982
F	0.527	0.539		0.374		0.320	0.350	0.361			0.260
Cl	0.035	0.035		0.048		0.049	0.079	0.061			0.067
S	0.003	0.003		0.005		0.038	0.041	0.004			0.007
[b]OH cal	0.435	0.423		0.573		0.592	0.531	0.574			0.666
H_2O cal(wt%)	0.780	0.758		1.026		1.060	0.950	1.027			1.192
[c]X_F	0.529	0.540		0.358		0.320	0.346	0.349			0.257
[c]X_{Cl}	0.036	0.036		0.048		0.051	0.080	0.061			0.068

[a] These data points are contaminated with clinopyroxene or felsic melt inclusion, shown here for the ease of identifying the zoning pattern. Other footnotes are the same as for Table 2.

before melt immiscibility. The crystallization of Fe-rich clinopyroxene, plagioclase and ilmenite from immiscible mafic melt will have a similar effect on the evolution of major elements, but cause further enrichment of incompatible elements, like P, Ba, K, REEs and Zr. Although the late-stage immiscible mafic melt has crystallized completely, the felsic melt has been preserved. Compositional variations of these late-stage felsic melts indicate that crystallization of the immiscible mafic melt is accompanied by compositional re-equilibration between the immiscible melt endmembers. The positive correlations between Al_2O_3, BaO and P_2O_5 contents in late-stage felsic melts suggest that these elements can be used as indices for the relative timing of entrapment, since incompatible elements become increasingly concentrated during immiscible mafic melt crystallization.

Being a late crystallizing mineral phase, apatite is found in the mesostasis regions of the sample. The close association between apatite and clinopyroxene, ilmenite, plagioclase, troilite, olivine, hyalophane, merrillite and Zr-bearing minerals (Figs. 1-3) suggests that they all crystallized from the late-stage immiscible mafic melt. This interpretation is supported by relative enrichment of Ti, Fe, Mn, Mg, Ca, Ba, P and Zr in the immiscible mafic melt (Fig. 10 and Table 5), and it does not contradict the notion that immiscible felsic melt maintains an equilibrium with the crystallization products of immiscible mafic melt, nor does it rule out the possibility that hyalophane, apatite and/or merrillite can crystallize from the immiscible felsic melt. Variations of element partitioning between the immiscible melt pairs and their crystallization during lunar basaltic evolution certainly deserve further experimental investigation. Our current understanding is that melt immiscibility enhanced the enrichment of incompatible elements in the immiscible mafic melt and promoted the saturation of phosphates, hyalophane and Zr-bearing minerals.

Theoretically speaking, sulfide saturation can happen at any stage of the melt evolution. In our samples, sulfide is mainly present in the mesostasis, suggesting that it is part of the crystallization product from the immiscible mafic melt. Large troilite crystals may be part of an earlier stage of crystallization along with clinopyroxene, ilmenite and plagioclase. The common coexistence of troilite and vapor voids (Fig. 1) suggests that the growth of troilite is contemporaneous with degassing. Degassing could well be a direct result of crystallization of the immiscible mafic melt. The $\delta^{34}S$ values of troilite in the CE5 basalts range from −1.6 ‰ to 2.0 ‰, showing both inter-grain and intra-grain variability, which has been suggested to be caused by degassing (Liu et al., 2022).

In summary, melt immiscibility, immiscible mafic melt crystallization, sulfide saturation and degassing are protracted processes during lunar basaltic evolution. It is important to take these processes into account when interpreting trace element and volatile records in both apatite and melt inclusions.

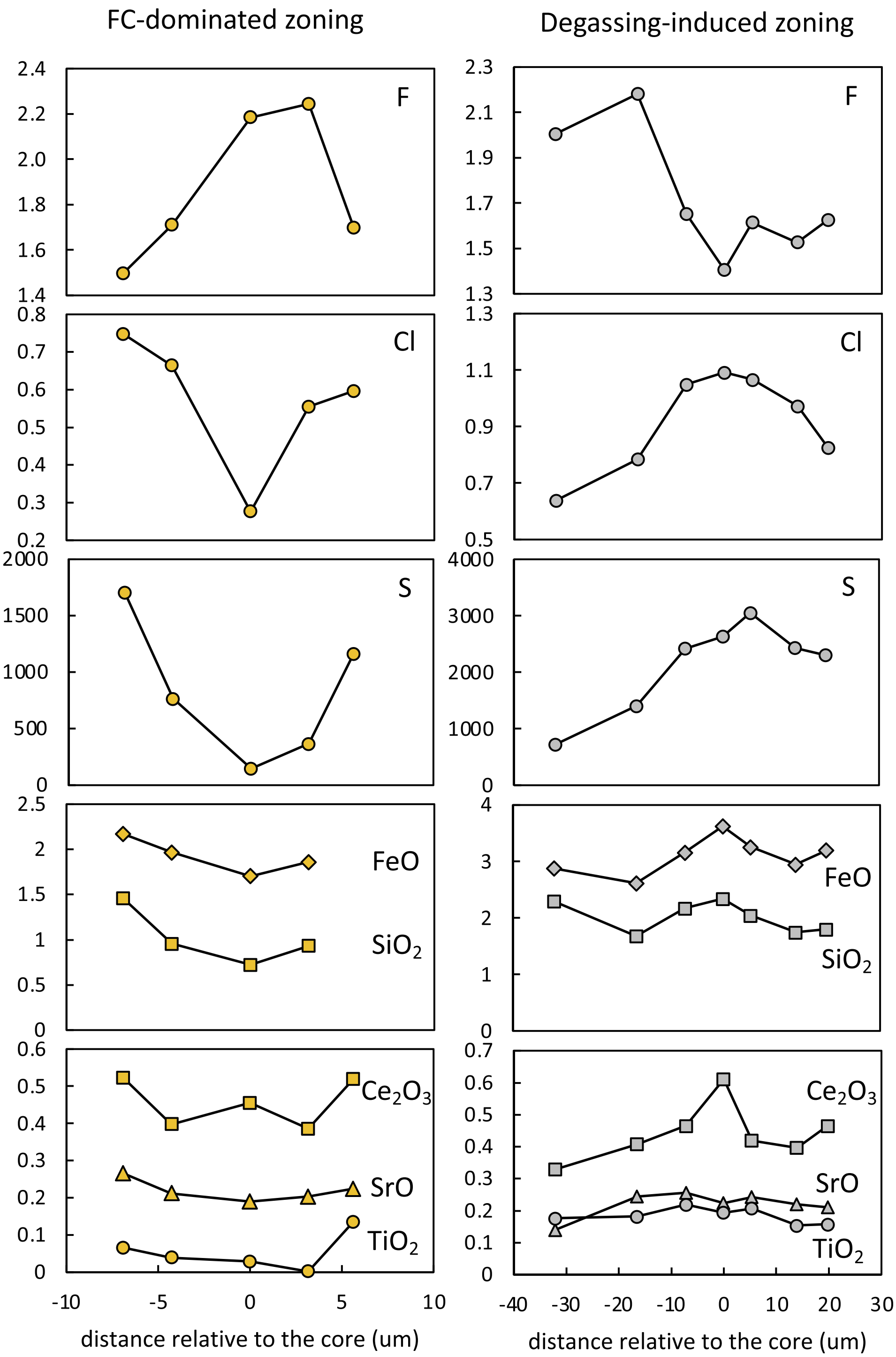

Fig. 5. Comparison of both volatiles and nonvolatile trace elements between fractional crystallization (FC)-dominated zoning (the left column) and degassing-induced zoning profiles (the right column) as shown in Fig. 4a and 4b. For the FC-dominated zoning, the relative core-to-rim positions are estimated with the third data point (No. 45) as the core; the fifth data point (No. 50) is contaminated with clinopyroxene, SiO_2 and FeO contents are therefore not plotted for this data point. For the degassing-induced zoning, the relative core-to-rim positions are estimated with the fourth data point (No. 34) as the core.

4.2. The coexistence of apatite and merrillite

The coexistence of apatite and merrillite is a common occurrence in lunar and Martian samples. As merrillite contains no H_2O, the presence of merrillite in lunar and Martian samples, and its absence in terrestrial samples, have been cited as evidence for H_2O depletion in lunar and Martian magmas relative to magmas on Earth (Jolliff et al., 2006; Patiño Douce et al., 2011). However, McCubbin et al. (2014) reported the coexistence of merrillite with OH-rich apatite (up to the equivalent of 8600 ppm H_2O) in the Shergotty Martian meteorite, suggesting that the presence of merrillite cannot be used as evidence for H_2O-poor magma. Through thermodynamic modeling, Patiño Douce and Roden (2006) demonstrated that the stability of apatite and merrillite depends on the activities of phosphorous and halogens, with the presence of merrillite indicating a depletion of halogens or enrichment of phosphorous or both.

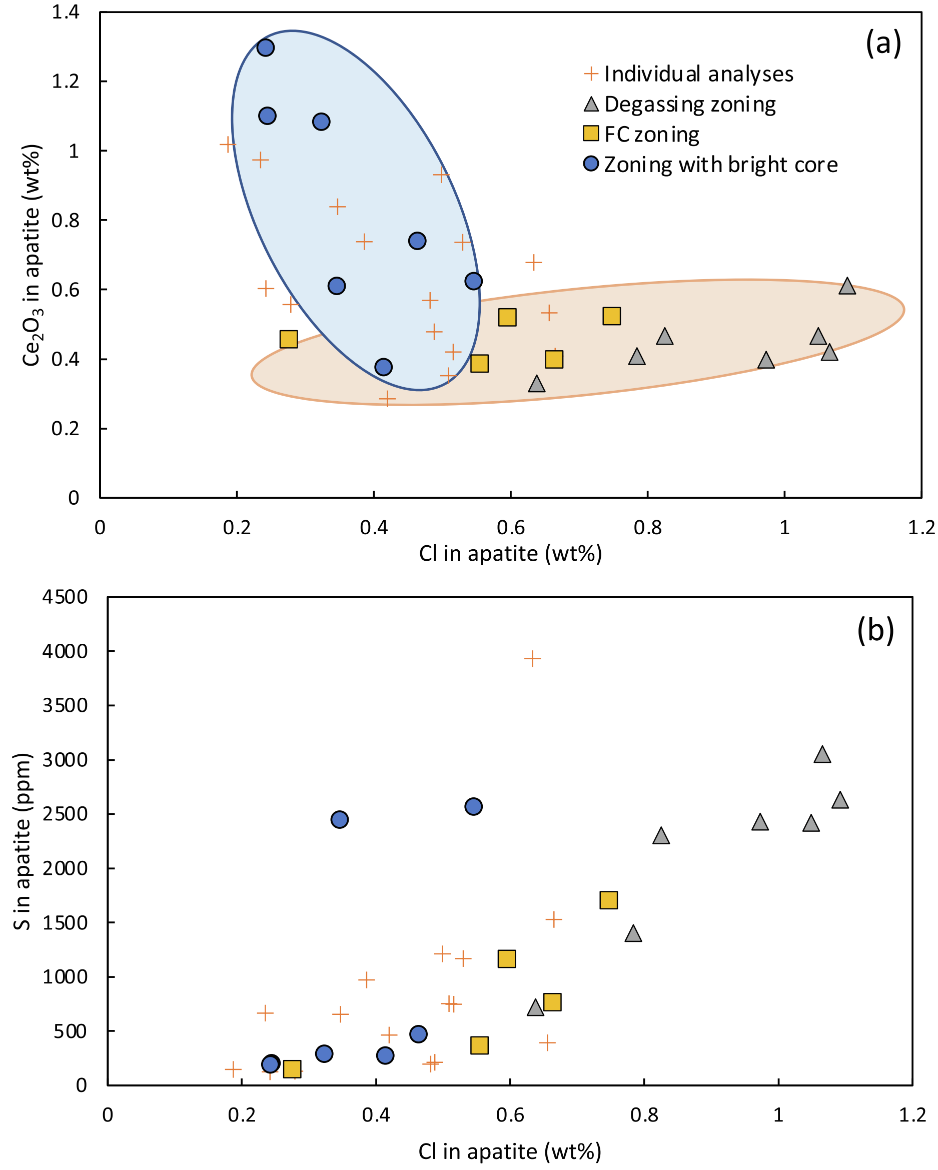

Fig. 6. (a) Ce_2O_3 versus Cl and (b) S versus Cl plots are used to showcase the variation of apatite compositions. Three different kinds of zoning profiles: fractional crystallization (FC), degassing and zoning with bright cores, are presented separately from individual analytical points.

The high FeO and low MgO contents in both apatite and merrillite found in our samples (Table 1-4) suggest their crystallization from a late-stage FeO-rich melt, which is likely to be the FeO-enriched mafic melt produced through immiscibility, consistent with textural evidence. Moreover, apatite grains in close proximity to merrillite have higher FeO contents (e.g., cluster No.23–26). This is also observed in samples reported by Hu et al. (2021); e.g., apatite from 406–015,014 has higher S and FeO contents than that from 406–015,001, while showing similar textures, the difference being the coexistence of merrillite in 406–015,014. Although this could reflect a local chemical character, another explanation is that the saturation of merrillite may occur later than that of apatite. This is consistent with the occurrence of merrillite as anhedral grains intergrowing with other mineral phases (Fig. 1d, 2, 3). The depletion of halogens due to apatite crystallization and degassing could result in the crystallization of merrillite/merrillite + apatite at a later stage of immiscible mafic melt crystallization.

Based on the analyses of apatite and merrillite grains in close vicinity, REE partition coefficients between merrillite and apatite are estimated to be around 10, in agreement with the reported values for merrillite with REE contents approaching saturation, i.e., 2REE per 56 oxygens (Jolliff et al., 1993). The high REE contents in merrillite also supports its crystallization from immiscible mafic melt. The enrichment of P and REEs in the immiscible mafic melt could be important contributing factors for merrillite saturation.

Our interpretations can be further demonstrated using the schematic phase diagram for merrillite and apatite crystallization presented in Patiño Douce and Roden (2006), with the fluorapatite endmember shown in Fig. 12 as an example. According to the analyses of Patiño Douce and Roden (2006), the F_2 and O_2 fugacity ratios ($\log(f(F_2)_{QFM}/f(O_2)^{1/2}_{QFM})$) increase in the order of Mars, Earth and the Moon, with average values of −0.578 ± 0.173, 0.042 ± 0.378, and 0.635 ± 0.238 based on the samples presented therein. The crystallization path for Mars may firstly reach merrillite crystallization, then apatite and merrillite co-crystallize at the pseudo-invariant point where the fugacity ratio between F_2 and O_2 is fixed. The magmatic evolution for lunar and terrestrial samples may reach the apatite phase boundary first, then in the case of lunar samples, devolatilization and increase of P_2O_5 activity could move the system towards merrillite saturation. The absence of merrillite in terrestrial samples suggests that the P_2O_5 activity was never high enough to reach merrillite saturation.

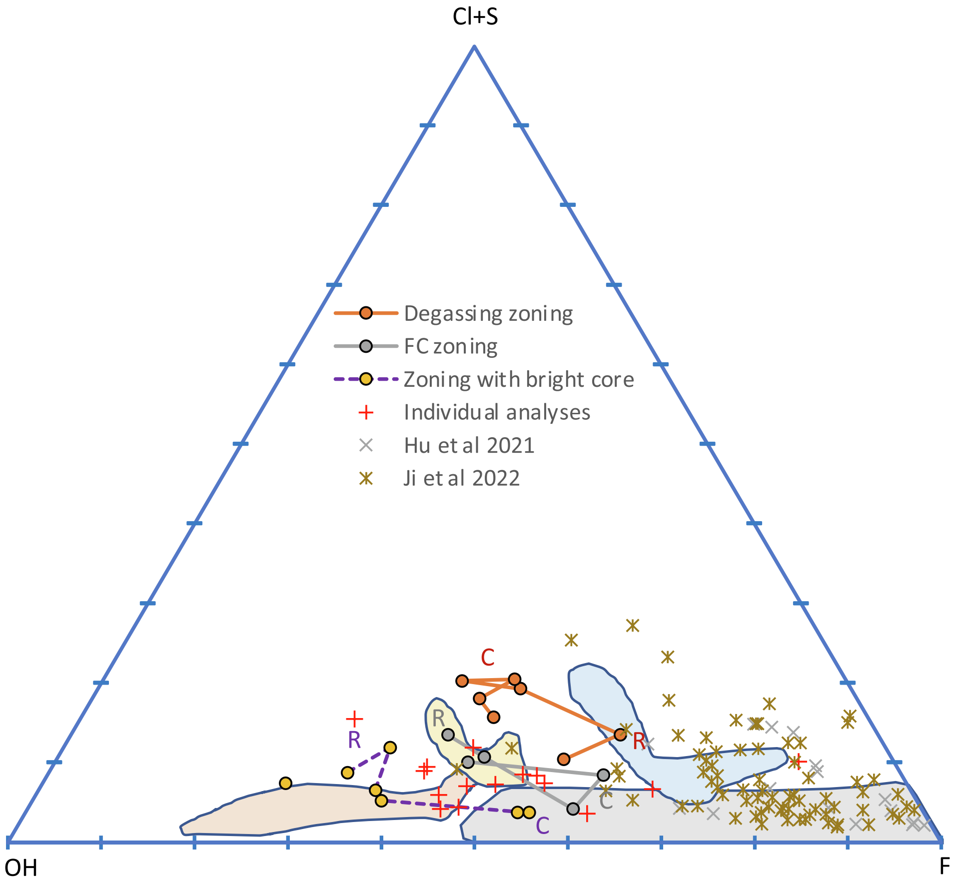

Fig. 7. Ternary plot for mole fractions of the F, Cl + S and OH apatite endmembers showcasing the variation of volatile contents in apatite. Considering the positive correlation between Cl and S, they are lumped together for illustrative purposes. The mole fraction of the OH endmember is estimated as OH=1-F-Cl-S. To distinguish them from individual analyses, data points of zoning profiles (rim-core-rim) are connected by solid lines, with letters “C” and “R” denoting the core and rim positions respectively. The data points for apatite with bright cores, were collected from different grains, but connected by dashed lines in a core to rim sequence, in order to better illustrate the differences between core and rim compositions. Previous analyses of apatite from a set of CE5 basaltic clasts by EPMA (Hu et al., 2021) and NanoSIMS (Ji et al., 2022) are plotted for comparison. The shaded region with light grey color represents previously reported apatite compositions compiled in McCubbin et al. (2023) for Apollo low-Ti and high-Ti mare basalt samples. Shaded regions with light salmon, yellow and blue colors represent apatite compositions reported previously for meteorites LAP 04841 by Tartèse et al. (2013) using EPMA, MIL 05035 by Joy et al. (2008) using EPMA and also MIL 05035 by Wang et al. (2019) using NanoSIMS, respectively.

4.3. *The evolution of apatite compositions*

The difference in zoning patterns, and general inter-grain variations of shapes, sizes and compositions suggest different generations of apatite crystallization. For example, the large apatite grain with FC-dominated zoning may have crystallized early from the immiscible mafic melt, with its core containing the lowest level of incompatible elements (e.g., 0.28 wt% Cl, 147 ppm S, 0.72 wt% SiO_2, 1.70 wt% FeO and 0.029 wt% TiO_2) among all apatite grains analyzed (Table 2). The observed increasing trends for nonvolatile elements in the FC-dominated zoning are consistent with the progressive enrichment of incompatible elements during the crystallization of late-stage immiscible mafic melt.

The higher incompatible element concentrations, e.g., Cl, S, FeO, SiO_2 and TiO_2, in the apatite grain displaying degassing-induced zoning, indicate that this apatite grain crystallized at a later stage than the apatite displaying FC-dominated zoning. The apatite grain with degassing-induced zoning lies next to a large vapor void, which supports the interpretation that its compositional zoning is due to the degassing process. As shown by the fractional crystallization modeling in section 4.5, apatite has such a strong preference for F that F content in apatite can still display a decreasing trend when there is H_2O degassing. The preservation of degassing zoning in this apatite grain may be attributed to its high Cl and S contents. One possibility is that significant Cl and S degassing occurs when Cl and S contents in melt are high enough after a certain degree of fractional crystallization. Another possibility is that the effect of degassing on apatite composition may be more prominent when the Cl and S contents in apatite are high. The decreasing Cl content in apatite due to degassing may be accompanied by decreasing REEs, SrO, and SiO_2 contents, considering that accommodation of REEs and SrO is favored in Cl-Ap endmember (Li and Hermann, 2017), and REEs and SiO_2 represent coupled substitutions for CaO and P_2O_5 in apatite. The higher TiO_2 content in this apatite and its close association with ilmenite may indicate the onset of ilmenite crystallization after the immiscible mafic melt reaches high enough TiO_2 content. An alternative explanation for the decrease in nonvolatile elements in the degassing profile may be a depletion of these elements in the surrounding residual magma due to the fast growth of apatite (Mollo and Hammer, 2017).

The medium-sized euhedral apatite grains with bright cores likely represent the main stage of apatite crystallization accompanying the enrichment of REEs in the evolving melt. Decreasing REE contents from core to rim, may be a result of the co-crystallization of merrillite or regional depletion of REEs during fast nucleation and growth of apatite. Decreasing F and increasing Cl and S contents from core to rim (Fig. 3 and Table 4) indicate the fractional crystallization progress, although the low values of Cl and S may reflect depletion as a result of previous degassing processes.

Both intra-grain and inter-grain compositional variations in apatite are common in previously reported Apollo samples, although detailed

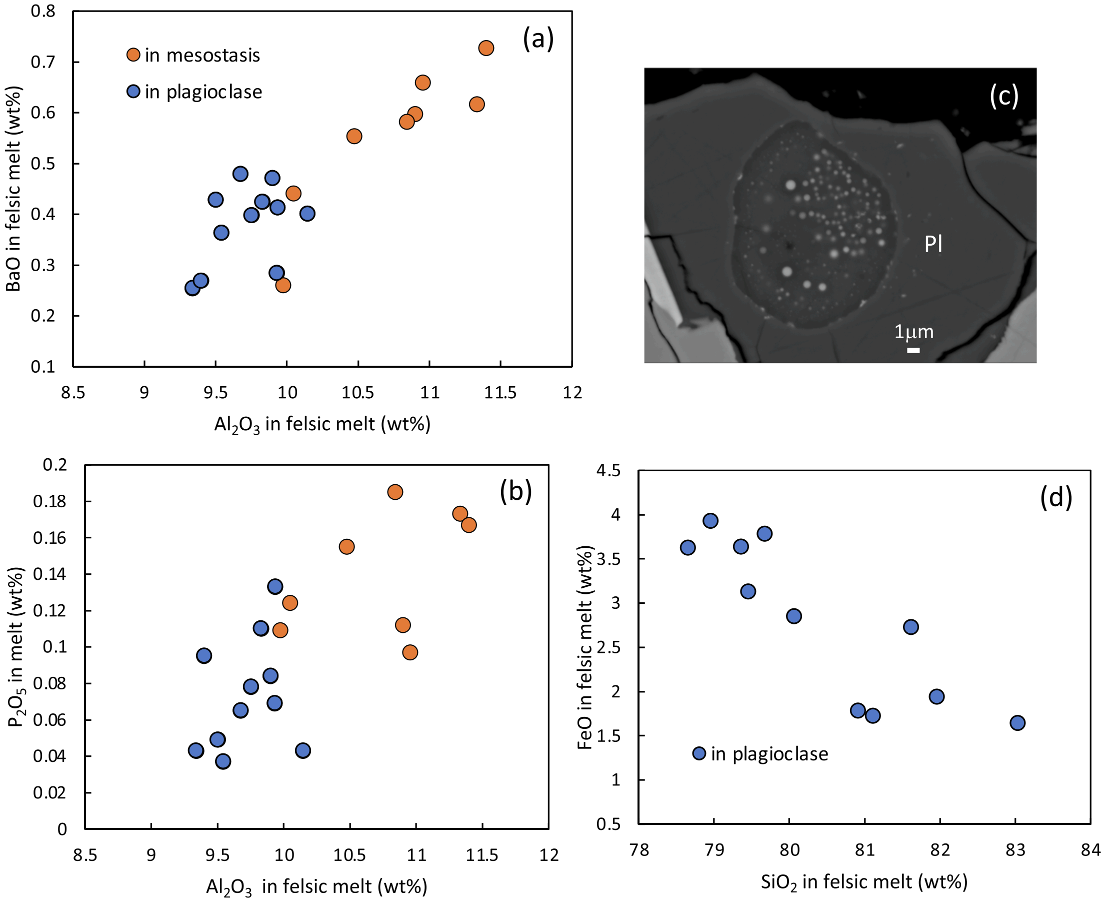

Fig. 8. (a, b) Positive correlations between Al_2O_3, BaO and P_2O_5 contents in felsic melt from clast 1. Note the differences between felsic melts contained in plagioclase and in the mesostasis. (c) BSE image showing the sub-micron bright spheres floating in felsic melt patches contained in plagioclase. (d) Negative correlation between SiO_2 and FeO contents for felsic melt patches in plagioclase, suggesting that these sub-micron bright spheres could represent immiscible mafic melt trapped in felsic melt patches.

studies of apatite zoning are rare (Greenwood et al., 2011; Boyce et al., 2014). Boyce et al. (2014) reported a fractional crystallization zoning profile (~400 μm long) in an apatite grain from Apollo sample 12039,42, with volatile concentrations varying in similar ranges, e.g., from core to rim, ~2–1 wt% for F, ~0.1–1 wt% for Cl and ~ 0.7–1.2 wt% for H_2O, but lower S contents (~0–600 ppm), compared to the FC-dominated zoning (~15 μm long) observed in our sample. This apatite grain coexists with decomposed olivine, pyroxene and plagioclase, likely formed before significant degassing, which explains its high volatile (H_2O, Cl and S) contents at the rim. The zoning pattern of medium-sized euhedral apatite grains, i.e., higher F, REEs, FeO and SiO_2 in the core and higher Cl in the rim, is similar to that reported for apatite in Nakhla by Martínez et al. (2023); which was interpreted to represent sequential crystallization from a melt that was becoming Cl-enriched due to assimilation of volatile-rich crustal sediments. However, such an explanation is unlikely to be applicable to CE5 basalt.

The preservation of apatite zoning in micrometer scale within our samples suggests fast growth of apatite. Similar observations have been reported for Cl and Cl isotopic compositions in CE5 apatite by means of NanoSIMS analyses (Ji et al., 2022). Both the tiny crystal size and compositional zoning reflect fast cooling during the last stage of lunar basaltic evolution. The patchy zoning and skeletal crystal shapes (Fig. 1e), in particular, reflect fast and numerous nucleation of apatite during the final stage of crystallization. Sometimes the skeletal apatite grains have only a shell (Fig. 1e), which may suggest a reversed crystallization, i.e., similar to the formation mechanism of hollow crystals. This represents an alternative explanation for the apatite zoning with bright cores or the degassing-induced zoning profile observed. Without further evidence, however, this remains speculation. If apatite grains with bright cores did crystallize inwards, the higher F and lower Cl and S contents in the core compared to the rim suggest a degassing process accompanying the fractional crystallization process.

4.4. *Sulfur solubility in lunar melt*

The high S contents (~2500 ppm) measured in immiscible mafic melts preserved in olivine and ilmenite in clast 2 are in agreement with their high FeO contents (>20 wt%) (Fig. 13a). The coexisting immiscible felsic melts have high S contents (~500 ppm) as well, which is in clear contrast to the low S contents (mostly < 100 ppm) measured in the late-stage felsic melts (Fig. 13a). As the immiscible melt pair found in olivine from clast 2 show coexistence with a troilite grain, the measured S contents in the melt pair may be considered as the sulfur content at sulfide saturation (SCSS) (Shima and Naldrett, 1975), i.e., the maximum S content that can be dissolved in melt when reaching sulfide saturation. The close association of felsic melt with both sulfide and vapor voids in the mesostasis suggests that the late-stage felsic melt may have experienced troilite saturation as well, possibly at the same time as degassing. If this is the case, we may ask the question why the SCSS values for the late-stage felsic melts are lower than that for the earlier-stage felsic melt found in olivine and ilmenite?

We used three different models from O'Neill (2021), Ding et al. (2018) and Liu et al. (2007) to calculate SCSS for the melt inclusions found in our samples (Fig. 13b, Table 5). The O'Neill (2021) model was calibrated based on experimental data for basic melts with FeO content > 1 wt%, while the model by Ding et al. (2018) was calibrated for

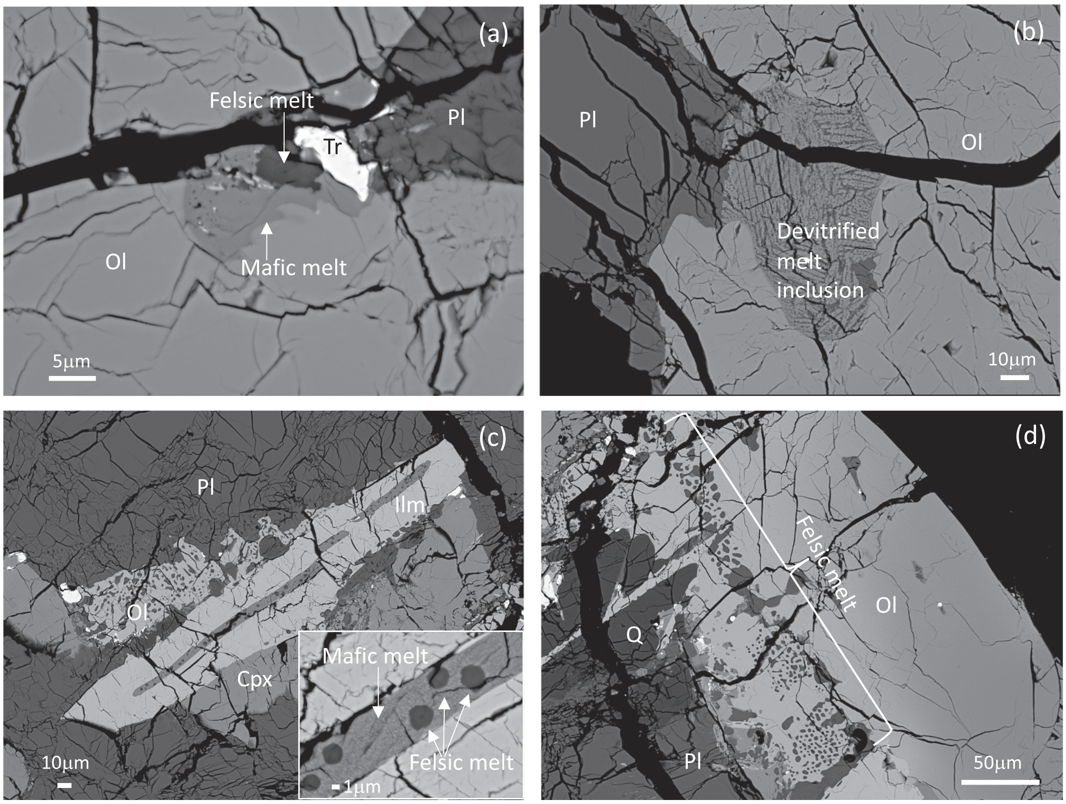

Fig. 9. BSE images showcasing the different kinds of melt inclusions found in clast 2. (a) An immiscible melt pair next to a troilite grain preserved in olivine. (b) Devitrified melt inclusion found in olivine. (c) An elongated melt inclusion showing immiscible felsic melt spheres floating in mafic melt, found in a large ilmenite lath. (d) Late-stage felsic melt inclusions contained in the Fe-rich portions of a large olivine grain.

basaltic melts with FeO contents > 5 wt%; both models address high FeO compositions (>15 wt%), and are therefore considered applicable to the immiscible mafic melts. The model of Liu et al. (2007) was calibrated for a wide range of melt compositions. To the best of our knowledge, it is the only model that included SCSS data for anhydrous felsic melt compositions. All three models require input parameters of pressure, temperature and melt composition. The pressure is set at 1 bar (He et al., 2022) and temperature is calculated using the magma thermometer of Putirka (2008) as suggested by O'Neill (2021), resulting in temperature estimations of ~1200 °C, ~1050 °C, ~1050 °C and ~900 °C for the melt pair in olivine, the melt pair in ilmenite, devitrified melt inclusions in olivine and late-stage felsic melt, respectively. The calculated SCSS values show a general comparability with measured S contents in melt, in support of the interpretation that sulfide saturation exerts the dominant control on S content in melt (Fig. 13b). The larger discrepancy between SCSS model prediction and S content in immiscible mafic melt is noteworthy (Fig. 13b), reflecting the difficulty in predicting SCSS in high-FeO mafic melt, with the predictions by Ding et al. (2018) being closest to the measured values. Calculated SCSS values for felsic melts by all three models are largely similar. However, only the O'Neill (2021) model predicted the high S content in the immiscible felsic melt found in olivine; with the other two model predictions being lower than the measured S content (Table 5). The high S content in this melt can be attributed to its low FeO content (~1 wt%) and high temperature conditions (~1200 °C estimated); while only the O'Neill (2021) model incorporated the negative correlation between S and FeO contents in melt when FeO content is < 5 wt%. Calculated SCSS values for the felsic melt in ilmenite by all three models are lower than the S content measured (Table 5). The H_2O effect has not been taken into consideration here; leading us to wonder whether its high S content can be attributed to a high H_2O content?

The good agreement between calculated SCSS values and the low S contents in late-stage felsic melts suggests that these low values represent sulfide saturated conditions (Table 5). In comparison to the high S contents in earlier-stage felsic melts in olivine and ilmenite, these lower values can be attributed to the lower temperature conditions, and also possibly lower H_2O content in melt after degassing.

4.5. *An explanation for high sulfur contents in lunar apatite*

Sulfur contents in apatite obtained in this study vary in a large range of ~ 130 ppm to ~ 3000 ppm, expanding previous reports on Apollo apatites (up to ~ 600 ppm) to much higher values. Although not their research focus, several previous studies reported apatite compositions from CE5 basalt with S contents up to ~ 2000 ppm (Che et al., 2021; Hu et al., 2021; Li et al., 2021). Moreover, we find that there is a positive correlation between FeO and S contents for apatite reported in both this study (Fig. 14a) and previous studies (Fig. 14b). The data points which deviate from the general positive correlation in Fig. 14a are from the bright cores of the medium-sized euhedral apatite grains. The FeO content in apatite may be considered as the "arrow of time", pointing out the direction of fractional crystallization.

During fractional crystallization, S content in melt increases due to the incompatible nature of S; however, unlike other volatiles, S content in melt is limited by the saturation of sulfide, which poses an upper limit on S content in melt, i.e., SCSS. The coexistence of apatite and sulfide in the mesostasis suggests that the immiscible mafic melt likely reached sulfide saturation when apatite started to crystallize. If S is treated as a trace element, the ten-fold increase of S content in FC-dominated zoning (Fig. 5) would be difficult to explain using Nernst partition coefficients (Konecke et al., 2017).

The positive correlation between Cl and S contents in apatite shown in the plot of all analytical points (Fig. 6b) and the synchronous increase or decrease of Cl and S contents in both the fractional crystallization and

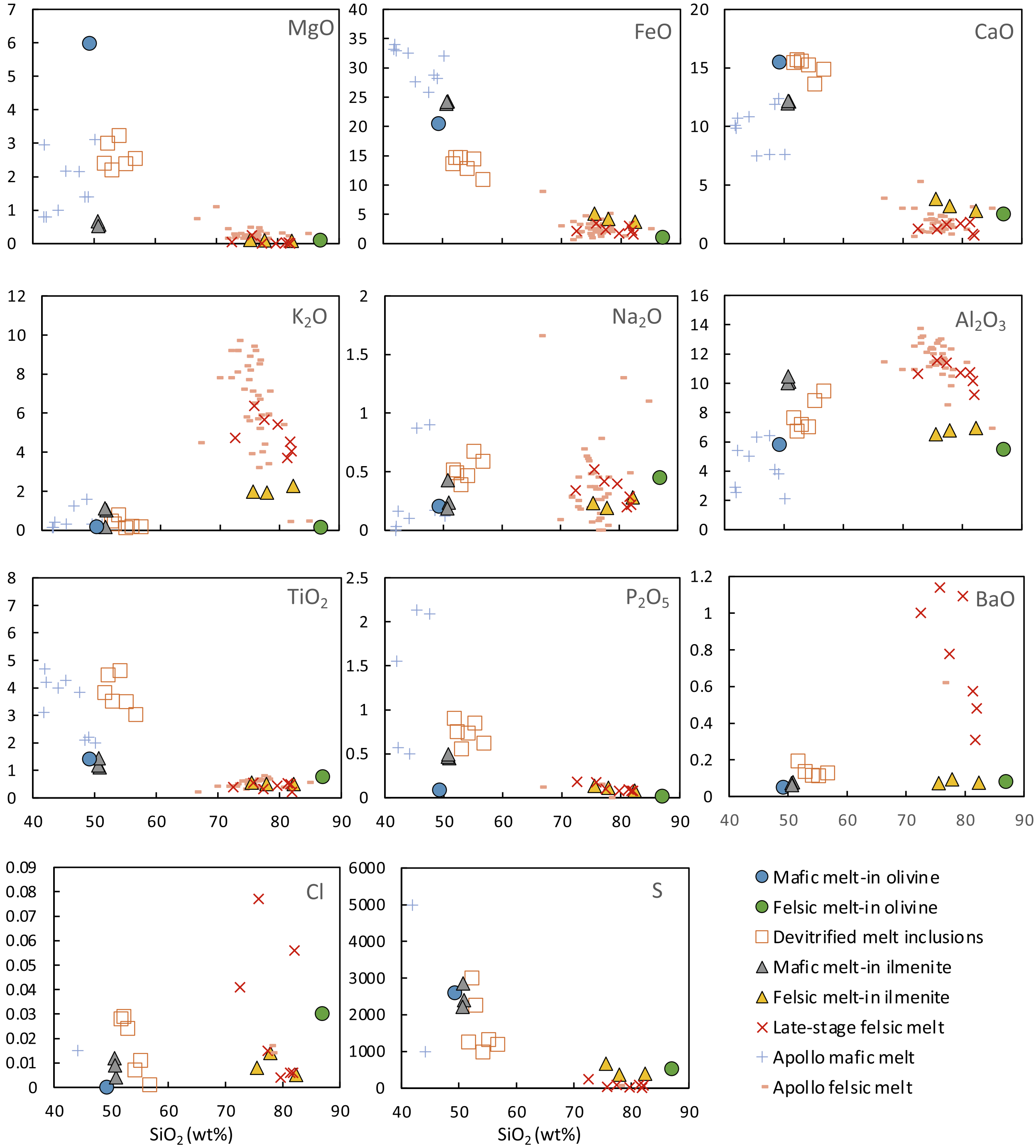

Fig. 10. Major element (in wt%) and volatile contents (Cl in wt% and S in ppm) plotted against SiO_2 content for the different kinds of melt inclusions found in clast 2 (as shown in Fig. 9). The immiscible mafic and felsic melt inclusions from Apollo samples were compiled by Zeng et al. (2020), including individual analyses of melt inclusions from Apollo 11 samples by Roedder and Weiblen (1970), and average compositions for melt inclusions from Apollo 11, 12 (Roedder and Weiblen, 1971; Shearer et al., 2001) and 14 (Snyder et al., 1993) samples.

degassing zoning profiles suggest that they behave similarly during fractional crystallization and degassing. Therefore, we propose that the high S contents in apatite may be explained by the fractional crystallization model proposed in Boyce et al. (2014).

If the core composition of the FC-dominated zoning profile can be considered to represent the apatite composition during the initial stage of saturation, and the immiscible mafic melt in ilmenite can be considered to represent the melt composition in equilibrium with this apatite, then we can estimate the S partition coefficient between apatite and sulfide-saturated mafic melt to be ~ 0.06, consistent with experimental values (Konecke et al., 2019); if the immiscible felsic melt is also in equilibrium with this apatite composition, an estimated S partition coefficient of ~ 0.3 is also in agreement with the experimental results (Konecke et al., 2017).

To test this idea, fractional crystallization modeling has been performed according to the method of Boyce et al. (2014), which employs the canonical fractional crystallization equation, but implemented with a step-wise recalculation of partition coefficients from apatite and melt equilibrium for each step; and apatite composition is calculated based on exchange coefficients. It is assumed that nominally anhydrous minerals

Table 5
Average compositions for different kinds of melt inclusions and corresponding SCSS values calculated with three different models.

Description	Clast 2-melt pair in olivine −mafic	Clast 2-melt pair in olivine −felsic	Clast 2-in olivine-devitrified	σ(5)	Clast 2-melt pair in ilmenite −mafic	σ(3)	Clast 2-melt pair in ilmenite −felsic	σ(3)	Clast 2-late-stage felsic melt	σ(7)	Clast 1-late-stage felsic melt	σ(19)
SiO_2	49.28	87.01	54.18	*1.96*	50.74	*0.12*	78.58	*3.46*	78.66	*3.58*	80.06	*1.68*
TiO_2	1.41	0.77	3.69	*0.59*	1.25	*0.17*	0.52	*0.04*	0.42	*0.12*	0.58	*0.22*
Al_2O_3	5.78	5.48	8.00	*1.07*	10.18	*0.25*	6.74	*0.22*	10.62	*0.79*	10.15	*0.64*
FeO	20.42	1.01	13.25	*1.51*	24.13	*0.22*	4.33	*0.72*	2.34	*0.67*	2.44	*0.80*
MnO	0.34	0.04	0.19	*0.04*	0.33	*0.03*	0.06	*0.02*	0.02	*0.01*	0.02	*0.01*
MgO	5.98	0.09	2.54	*0.39*	0.58	*0.07*	0.10	*0.02*	0.05	*0.08*	0.01	*0.01*
CaO	15.47	2.49	14.95	*0.79*	12.10	*0.10*	3.27	*0.50*	1.31	*0.44*	1.00	*0.19*
Na_2O	0.20	0.45	0.52	*0.11*	0.28	*0.13*	0.23	*0.04*	0.34	*0.12*	0.24	*0.06*
K_2O	0.17	0.15	0.35	*0.28*	0.77	*0.52*	2.06	*0.19*	4.92	*0.94*	3.60	*0.63*
BaO	0.05	0.08	0.14	*0.03*	0.07	*0.01*	0.08	*0.01*	0.77	*0.32*	0.45	*0.14*
P_2O_5	0.09	0.01	0.73	*0.15*	0.47	*0.02*	0.11	*0.03*	0.11	*0.05*	0.10	*0.05*
Cl		0.03	0.01	*0.01*	0.008	*0.004*	0.009	*0.005*	0.03	*0.03*	0.005	*0.004*
Total	99.26	97.63	98.60	*1.12*	100.92	*0.33*	96.11	*2.67*	99.61	*2.98*	98.69	*0.81*
S(ppm)	2596	528	1399	*493*	2497	*331*	479	*161*	82	*80*	102	*98*
SCSS model predictions												
P(bar)	1	1	1		1		1		1		1	
T(°C)	1200	1200	1050		1050		1050		900		900	
O'Neill 2021	5071	409	1945		3605		171		65		59	
Liu et al 2007	3405	162	1319		1594		322		99		84	
Ding et al 2018	3775	221	1406		2121		236		109		95	

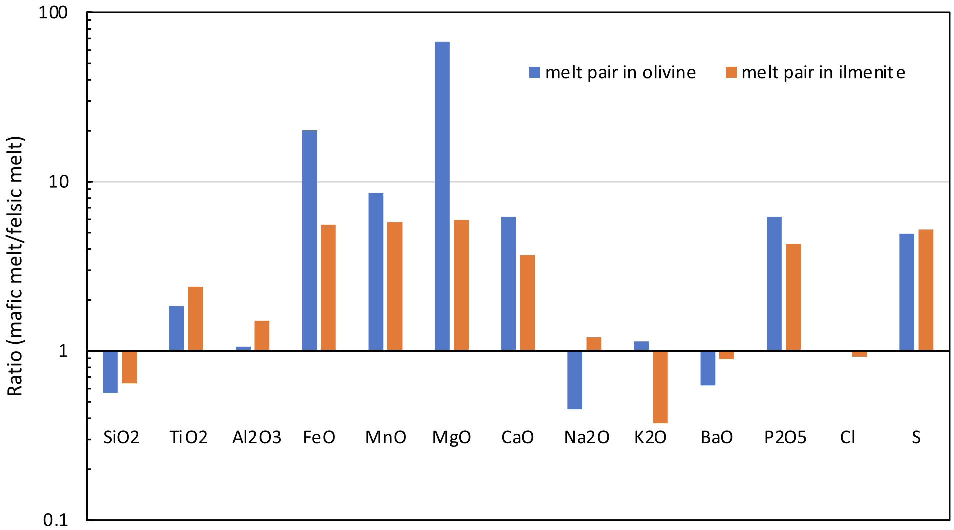

Fig. 11. Oxide and volatile ratios between immiscible mafic and felsic melt pairs in olivine and ilmenite of clast 2.

(NAMs) contain no F, Cl and H_2O, the parental melt contains 70 ppm F, 40 ppm Cl, 1500 ppm H_2O and 760 ppm S (see section 4.7 for derivation of these values), and apatite reaches saturation after ~90 % crystallization and ~ 90 % degassing. In this simplified scenario, the volatile contents of the immiscible mafic melt from which apatite crystallized, would be similar to the parental melt, although melt immiscibility may cause volatile fractionation, the degree to which is unconstrained. The exchange coefficients between F-Cl-H_2O from McCubbin et al. (2015a) have been used in the modeling. To incorporate S, the exchange coefficient between Cl and S, K_d(Cl-S), has been estimated to be 100 ± 70 based on the average partition coefficients for Cl and S, 2 ± 1 and 0.02 ± 0.01, from McCubbin et al. (2015a) and Konecke et al. (2019), respectively. By assuming P_2O_5 content in excess, that is, the amount of apatite crystallized is limited by the volatile contents, we modeled the evolution of F, Cl, H_2O and S contents in melt and apatite between 90 %-91 % crystallization with results shown in Fig. 15. We see a monotonic decrease of F (70–13 ppm) and Cl (40–30 ppm), and a slight increase of H_2O (1500–1625 ppm) and S (760–843 ppm) in melt. The modeling results for apatite reproduce the decreasing F and increasing H_2O profiles of the FC-dominated zoning found in our sample and reported for Apollo sample 12039,42 in Boyce et al. (2014). The modeling results also predict increasing Cl and S contents in apatite; however, the magnitude of Cl increase (up to 0.4 wt%) is lower than that observed in both our sample and Apollo sample 12039,42 (0.8–0.9 wt%). While the magnitude of S increase matches that for the FC zoning in Apollo sample 12039,42 (up to ~ 600 ppm), it is lower than that in the FC-dominated zoning in our sample (up to ~ 1700 ppm at the rim).

As shown in Fig. S3 of Boyce et al. (2014), the trend of variation for F, Cl, H_2O and S in apatite depends on the relative abundances between F, Cl, H_2O and S in the initial melt, while the absolute contents only determine how far apatite crystallization will progress. The decreasing F and increasing Cl, H_2O and S contents in apatite reflect the preference of apatite for F, and the rise in concentration occurs in the sequence of Cl, H_2O and then S, simply because the values of partition coefficients between apatite and melt decrease in the order of $D_F > D_{Cl} > D_{H2O} > D_S$. There is currently no experimental constraint on exchange coefficients

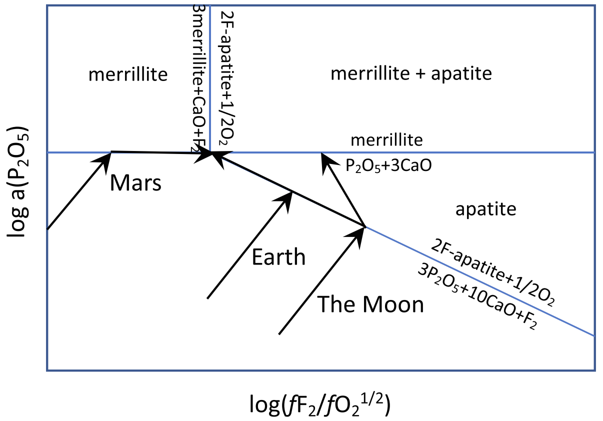

Fig. 12. Schematic phase diagram for merrillite and apatite (F–Ap shown here) crystallization as a function of the activity of P_2O_5 and the fugacity ratio between F_2 and O_2. Adapted from Fig. 9 in Patiño Douce and Roden (2006). Possible evolutional paths for Mars, Earth and the Moon are shown using arrows, see text for details.

involving S, however, increase of partition coefficients for Cl and S can increase the Cl and S contents in apatite for the whole profile, but not the magnitude of increase along the profile. One possible solution to enhance the magnitude of Cl and S increase in apatite is by degassing loss of H_2O, the effect of which is demonstrated by manually setting the H_2O content in melt to decrease in even steps to 500 ppm (Fig. 15 e-h). The magnitude of Cl and S increase along the profile is reproduced in this case (Fig. 15g). As S is less affected by degassing, we may set the S content in melt at apatite saturation at 2500 ppm, i.e., the SCSS for mafic melt; and it remains this figure during fractional crystallization. Such a revision produces higher S contents along the profile, and is able to reproduce the highest S contents measured in our sample (Fig. 15h). The above solutions are plausible considering that apatite is likely to record the convolution of fractional crystallization and degassing during the late stage of lunar basaltic evolution. Hu et al. (2021) reported H isotopic analyses of apatite from several CE5 basaltic clasts, with δD values ranging from 275±85 ‰ to 1022±87 ‰, supporting coeval apatite crystallization with degassing.

4.6. *Implications for the compositional and isotopic variations of lunar apatite*

In comparison to apatite compositions reported for Apollo high-Ti and low-Ti mare basalts, apatite compositions obtained from clast 1 show relatively low F and high Cl characteristics, similar to the apatite compositions reported for meteorites LAP 04841 (Tartèse et al., 2013) and MIL 05035 (Joy et al., 2008). Moreover, LAP basalts are low-Ti, low-Al and low-K basalts, but significantly more ferroan and enriched in REEs compared to Apollo 12 and 15 low-Ti basalts (Anand et al., 2006; Day et al., 2006; Joy et al., 2006; Hill et al., 2009). They mainly consist

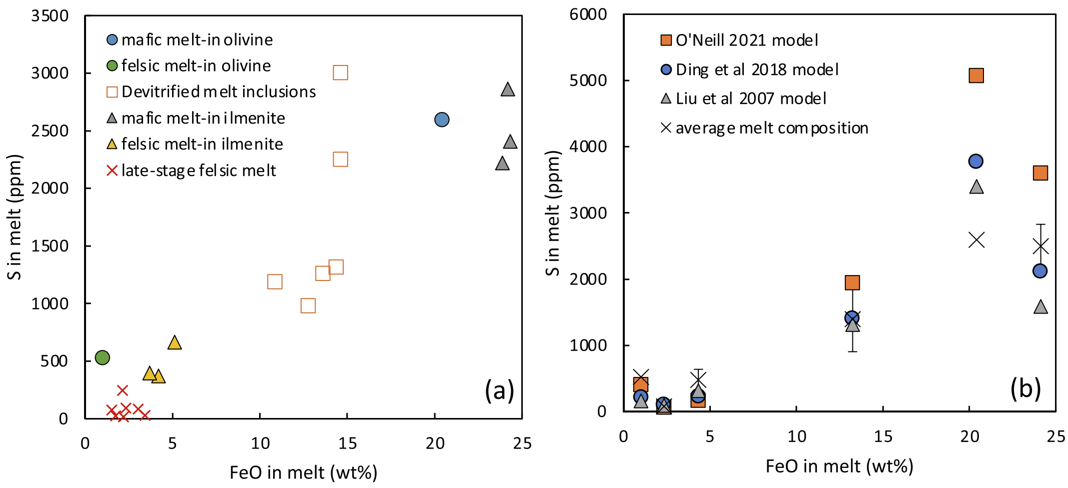

Fig. 13. (a) S contents measured in different melt inclusions from clast 2 plotted against FeO content. (b) Comparison between model predictions and average S contents measured for different melt inclusions from clast 2.

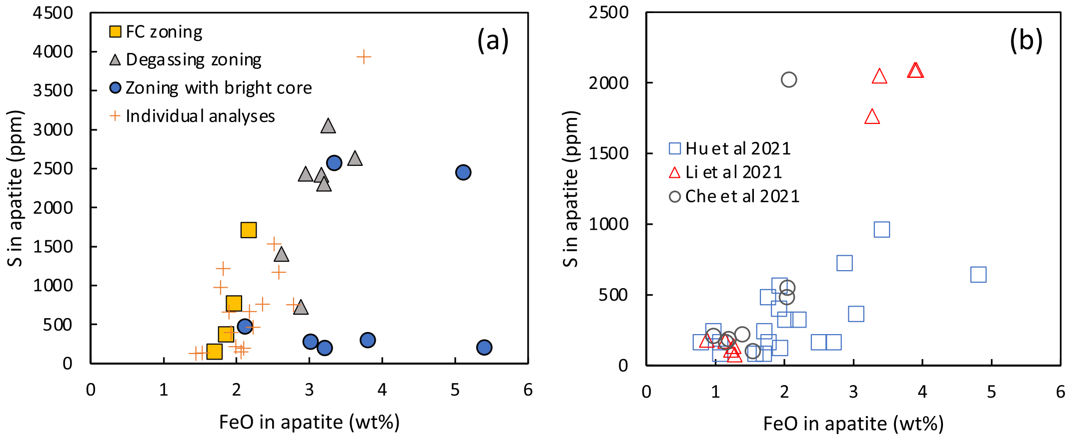

Fig. 14. Positive correlations between S and FeO contents in CE5 apatite for data reported in both this study (a) and previous studies (b).

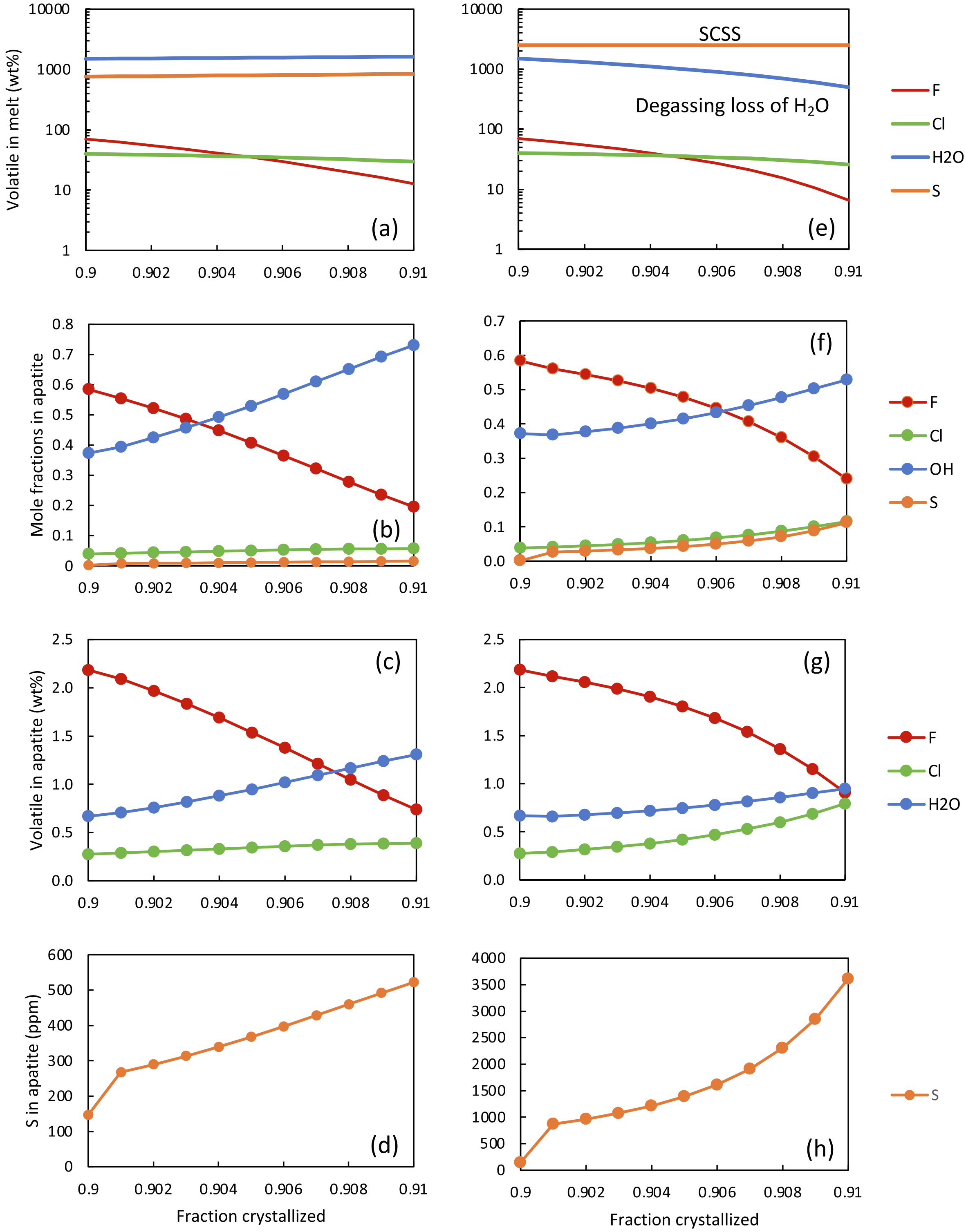

Fig. 15. (a-d) Fractional crystallization modeling results for F, Cl, H_2O and S contents in melt and apatite between 90–91 % crystallization. The modeling method is adapted from Boyce et al. (2014), with apatite saturation set at ∼90 % crystallization after ∼90 % degassing, and melt containing 70 ppm F, 40 ppm Cl, 1500 ppm H_2O and 760 ppm S. (e-h) The effects of degassing and sulfide saturation are investigated by setting melt H_2O content to decrease in even steps, and melt S content at 2500 ppm, i.e., the SCSS for immiscible mafic melt. Results are shown in the right column for comparison. Note the greater magnitude of increase for Cl and S in apatite in the latter case as a result of H_2O degassing.

of pyroxene, plagioclase and ilmenite, with only minor amounts of olivine and silica. Such evolved compositional characteristics for LAP basalts are also similar to that of clast 1. MIL 05035 is low- to very-low-Ti basalt composed mainly of pyroxene and plagioclase, with depleted incompatible trace element concentrations, akin to other Apollo very-low-Ti basalts (Joy et al., 2008; Liu et al., 2009). Therefore, the relatively low F and high Cl characteristics of apatite may be related to the evolved compositional character of the host basalt. Similarly, petrogenetic models invoking low degrees of partial melting and high degrees of fractional crystallization have been proposed to explain the evolved composition and enriched REE concentrations of CE5 basalt (Tian et al., 2021) and LAP basalts (Day et al., 2006; Elardo et al., 2015).

Considering all apatite data shown in Fig. 7 together, there are two different trends, one is represented by apatite compositions from Apollo low-Ti and high-Ti basalts, showing mainly the exchange between F and OH in apatite; the other is represented by apatite compositions with higher Cl contents, e.g., MIL 05035, the FC zoning and also the degassing zoning profiles, which is dominated by the exchange between F and Cl. The F-OH exchange trend suggests H_2O>F>Cl in melt during fractional crystallization, while the F-Cl exchange trend reflects H_2O>Cl > F in melt (McCubbin et al., 2015b) and possibly the contribution of degassing processes (McCubbin et al., 2016). Our fractional crystallization modeling results support that apatite compositional evolution is dominated by decreasing F and increasing H_2O contents during fractional crystallization when melt has H_2O>F>Cl (Fig. 15c) and H_2O degassing can cause an increase of Cl in apatite (cf. Fig. 15c and 15 g).

It is noteworthy that a gradual degassing of H_2O did not cause a drop of H_2O content in apatite, but a lower magnitude of increase along the fractional crystallization profile, while F content in apatite still displays a decreasing trend (Fig. 14g). This demonstrates the strong preference for F by apatite, that is, the fractional crystallization zoning is likely to dominate when degassing is not significant enough to alter such a trend. This can lead to a positive correlation between δD values and H_2O content in apatite, such as seen in lunar meteorite MIL05035 (Tartèse et al., 2013) and mare basalt samples 10044 and 12064 (Barnes et al., 2013). Chlorine isotopic compositions of CE5 apatite are reported to vary from 4.5 to 18.9 ‰, showing a positive correlation with Cl content (820–11989 ppm, measured by NanoSIMS) (Ji et al., 2022). Such a counterintuitive positive correlation can be explained by degassing loss of H_2O combined with a lesser extent of Cl loss during apatite crystallization.

4.7. *Volatile contents in the CE5 parental melt inferred from apatite compositions*

As the main volatile-bearing mineral in lunar samples, apatite composition can provide information regarding the volatile contents in melt at apatite saturation, based on the assumption of apatite-melt equilibrium. The volatile contents in the parental melt can then be calculated if the percentage of crystallization before apatite saturation is known. After recognizing the Non-Nernstian partitioning behavior of F, Cl and H_2O between apatite and melt (Boyce et al., 2014; McCubbin et al., 2015a; Li and Hermann, 2015), the consensus now is to employ exchange coefficients, in combination with an estimated concentration for one of the volatiles in the parental melt, F is recommended as it is least affected by degassing, in order to obtain the concentration values for other volatiles (McCubbin et al., 2015a). The inherent assumption here is that the volatile ratios are the same between the parental melt and melt at apatite saturation. The application of this method has proven to be quite useful in combination with melt inclusion studies for constraining the volatile budget, H_2O in particular, in planetary bodies (e.g., McCubbin et al., 2012; Gross et al., 2013; Tartèse et al., 2013; McCubbin et al., 2015b; McCubbin et al., 2016).

We used the core composition of the FC-dominated zoning profile, which has the lowest incompatible element concentrations (Table 2) and may represent the earliest crystallized apatite, to estimate volatile contents in parental melt and the mantle source. Due to the lack of constraints on the immiscible mafic melt apatite has crystalized from, we adopted the recommended approach from McCubbin et al. (2015a), which also enables direct comparison with results presented previously for Apollo samples. Using the exchange coefficient (K_d) values determined experimentally by McCubbin et al. (2015a), the F/Cl, Cl/H_2O and F/H_2O ratios (on a weight basis) in melt are estimated to be 1.66 ± 0.24, 0.025 ± 0.008 and 0.046 ± 0.007, respectively. The bulk F content in clast 1 is estimated to be 72 ± 21 ppm, based on the mass fraction of apatite (~0.4 %) and its average F content (~1.8 ± 0.5 wt%); it can then be derived that Cl and H_2O contents in the parental melt are ~ 43 ± 14 and ~ 1576 ± 518 ppm, respectively. The effect of exchange coefficients on volatile estimation can be demonstrated by using the formula proposed by Li and Costa (2020) (https://apthermo.wovodat.org/). The results for estimated Cl contents in parental melt are generally higher, 67–83 ppm for 1050 °C-950 °C conditions and H_2O contents are estimated to be between 0.1–0.2 wt%, which are in broad agreement with results using exchange coefficients from McCubbin et al. (2015a).

The estimated F content in CE5 parental melt falls in the range measured in olivine-hosted melt inclusions from Apollo mare basalts, mostly between ~ 30 ppm and ~ 140 ppm (Hauri et al., 2011; Chen et al., 2015; Ni et al., 2019), while higher values between 150–580 ppm were reported for melt inclusions from lunar basalt 12040 (Ni et al., 2019). The estimated Cl content is much higher than that reported for olivine-hosted melt inclusions from Apollo mare basalts, mostly ~ 1 to 11 ppm, with an approximate average value of ~ 4 ppm (Hauri et al., 2011; Ni et al., 2019; Stephant et al., 2019). However, higher values between ~ 3–78 ppm were measured in pyroxene-hosted melt inclusions by Stephant et al. (2019); correction for post-entrapment crystallization results in a range of ~ 1.3–38 ppm. Reported H_2O contents in olivine-hosted melt inclusions vary in large ranges of 3–740 ppm (Hauri et al., 2011; Saal et al., 2013; Chen et al., 2015; Wetzel et al., 2015; Singer et al., 2017; Ni et al., 2019; Stephant et al., 2020), with higher values up to 1410 ppm obtained in pyroclastic sample 74220 (Hauri et al., 2011). The F/H_2O ratio estimated for the CE5 parental melt, 0.046 ± 0.007, is similar to the lower end of values for olivine-hosted melt inclusions from 74220 and low-Ti mare basalts. However, the F/Cl ratio of 1.66 ± 0.24 is much lower than those measured in melt inclusions, e.g., the average value is 15 ± 2 for low-Ti basalts and 20 ± 3 for high-Ti basalts (McCubbin et al., 2023).

One of the basic assumptions of the McCubbin method is that volatile ratios are the same between the parental melt and melt in equilibrium with the chosen apatite composition. Due to apatite compositional evolution during fractional crystallization, it is necessary to use the composition of the earliest crystallized apatite for volatile estimation. The core composition of the FC-dominated zoning profile is chosen considering that it has the lowest nonvolatile incompatible elements and one of the highest F contents (Table 2). Naturally this composition may not represent the initial apatite saturation and the H_2O content calculated from stoichiometry may be overestimated, both factors can lead to an overestimation of Cl and H_2O contents and an underestimation of F content in melt. Note that the two data points with anomalously high F contents of 2.93 wt% (No. 3) and 3.83 wt% (No. 8) are located close to vapor voids and can be eliminated as early crystallized grains based on their high incompatible element concentrations (Table S2).

Another important factor to consider is possible volatile fractionation caused by fractional crystallization, degassing and melt immiscibility before apatite saturation. During fractional crystallization, the fractionation between F, H_2O and Cl is limited. For example, at 90 % crystallization, the enrichment of F and H_2O with a bulk partition coefficient of ~ 0.1 (Hauri et al., 2006; O'Leary et al., 2010; Beyer et al., 2012; Rosenthal et al., 2015; Potts et al., 2021) is around 8 times; while the enrichment factor of Cl with a bulk partition coefficient of ~ 0.001 (Potts et al., 2021) is around 10 times. The Cl content estimated in the parental melt is of the same magnitude as the bulk Cl content derived from the average apatite composition and its mass fraction, 22 ± 10 ppm; but the bulk H_2O content is much higher than that contained in apatite (30 ± 9 ppm), suggesting ~ 98 % degassing loss of H_2O in the sample. These values indicate differential degassing during the late-stage evolution of lunar basalt and apatite crystallization. Any degassing before apatite saturation will lead to underestimated volatile contents in the parental melt, and in the case of differential degassing, lower Cl/F and H_2O/F ratios. Our limited data on volatile contents in immiscible melt inclusions cannot provide definitive evidence regarding volatile fractionation during melt immiscibility. Considering the chemical properties of halogens, that is, F forms species in aluminosilicate glasses with Al, Na and Si, while Cl associates with network-modifying cations in melts (see the review by Aiuppa, 2009), we anticipate an increase of Cl/F ratio in immiscible mafic melt and an increase of F/Cl ratio in immiscible felsic melt. However, experimental data from McCubbin and Ustunisik (2018) suggest indistinguishable fractionation between F and Cl, and both F and Cl preferentially partition into the immiscible mafic melt with partition coefficients between 0.4–0.5 when the immiscible melt endmembers have a SiO_2 content difference of 25–30 wt% (see their Fig. 2). To settle this matter will require both analyses of immiscible melt inclusions with increased precision and further experimental investigation of volatile partitioning between immiscible melts.

4.8. *Implications for volatile estimations in the lunar mantle*

The major element compositions of CE5 basalt have been explained successfully by ~ 10 % partial melting of a hybrid mantle source composed of 80 % olivine + orthopyroxene and 20 % clinopyroxene + ilmenite, followed by 30–70 % fractional crystallization (Su et al., 2022). By adopting such a model with a fractional crystallization percentage of ~ 50 % estimated for the bulk composition of clast 1, F, Cl and H_2O contents in the lunar mantle source are estimated to be in the ranges of ~ 2.5–4.6, ~1.4–2.8 and ~ 53–105 ppm, respectively.

Another issue deserving consideration is the fractionation of volatiles during low degree partial melting of the lunar mantle. In the case of 10 % partial melting, adopting a partition coefficient of 0.1 for F and H_2O, and 0.001 for Cl (Potts et al., 2021), will lead to a relative enrichment of Cl in the melt, that is, the F/Cl ratio in the melt will be about half that in the mantle source. A correction for such a Cl enrichment results in lower Cl estimates in the lunar mantle, ~0.7–1.4 ppm.

Unlike F, Cl and H_2O, the S budget in lunar basalt is dominated by sulfide. Based on the fraction of sulfide, bulk S contents for the two clasts are estimated to be ~ 760 ppm and ~ 1720 ppm, respectively (Wang et al., 2023). Similar estimations have been made for the two CE5 basaltic clasts reported in Che et al. (2021), with values of ~ 1100 and ~ 1340 ppm, respectively. Measured S contents in melt inclusions in our samples lend support to such a range of estimations. Sulfur contents measured in melt inclusions from various Apollo lunar basalts mostly fall in a similar range of ~ 440–1500 ppm, although the low values may be affected by sulfide crystallization (Ni et al., 2019). According to the bulk S content of ~ 760 ppm for clast 1 and the model proposed by Su et al. (2022) with an estimated fractional crystallization percentage of ~ 50 %, the S content in the mantle source is estimated to be ~ 38 ppm. The SCSS value for immiscible mafic melt, i.e., 2500 ppm, may provide an upper limit for the S content in parental melt, which results in an estimation of ~ 125 ppm in the mantle source. When experimentally determined exchange coefficients involving S become available, S can also be used in the place of F as a reference for the estimation of other volatiles in melt.

The estimated H_2O content in the CE5 basalt mantle source is much higher than the previous estimate (1–5 ppm) based on melt inclusion analyses (283 ± 22 ppm H_2O with a δD value of −330 ± 170 ‰) by Hu et al. (2021). Liu et al. (2022) estimated a bulk S content of ~360 ± 180 ppm for CE5 basalt, and ~600 ± 300 ppm in the parental melt as $\delta^{34}S$ values in sulfide suggest ~ 40 % loss of S. They estimated the S content in the mantle source to be ~ 1–10 ppm. Both studies drew inferences on volatile contents in the lunar mantle based on the model of Tian et al. (2021), which proposed that 2–3 % partial melting of a mantle source composed of 86 PCS+2% TIRL (PCS, percent crystallized solid; TIRL, trapped instantaneous residual liquid), followed by 43–88 % fractional crystallization of the primary magma, can explain the REE distribution patterns in CE5 basalts. If we also adopt the petrogenetic model for CE5 basalt by Tian et al. (2021), the estimated volatile abundances in the mantle source will be 5–10 times lower, more in alignment with aforementioned two studies. Based on the average H_2O content (1921 ± 910 ppm by NanoSIMS) and mass fraction of apatite (~0.4 %), and ~ 98–99 % H_2O degassing loss that is required to enhance δD values in apatite from about − 330 ‰ to about + 600 ‰, Hu et al. (2021) estimated the H_2O content in the CE5 parental magma to be 600 ± 400 ppm, with the higher end value similar to our estimate for the parental melt of clast 1.

Considering the drastically different estimates derived from the two petrogenetic models for CE5 basalt, the estimates using the model of Su et al. (2022), ~2.5–4.6 ppm for F, ~0.7–1.4 ppm for Cl, ~53–105 ppm for H_2O and ~ 38–125 ppm for S, may represent the upper end estimations for volatile contents in the CE5 basalt mantle source, while the 5–10 times lower estimates based on the model of Tian et al. (2021) are more in agreement with the degree of volatile depletion in the Moon relative to the Earth (Ni et al., 2019; Zhang, 2020; McCubbin et al., 2023). The set of higher values show similarites to that for depleted Earth mantle, e.g., 16 ± 3 ppm F, 1 ± 0.5 ppm Cl, 142 ± 85 ppm H_2O and 146 ± 35 ppm S proposed in Saal et al. (2002); 11.0 ± 4.5 ppm F, 0.51 ± 0.09 ppm Cl, 116 ± 58 ppm H_2O, and 119 ± 30 ppm S estimated by Salters and Stracke (2004). The set of higher values align with estimations made for primitive lunar mantle based on F/Nd, Cl/K, H_2O/Ce and S/Dy ratios in olivine-hosted melt inclusions, e.g., ~5 ppm F, ~0.39 ppm Cl, ~84 ppm H_2O and ~52-120 ppm S by Ni et al. (2019). Similarly, based on F/Nd, Cl/Ba, H_2O/Ce and S/Dy ratios in olivine-hosted melt inclusions from pyroclastic sample 74220 and high-Ti, low-Ti mare basalts, McCubbin et al. (2023) estimated the primitive lunar mantle contains 3.1–4.9 ppm F, 1.0–4.1 ppm Cl, 1.38–74 ppm H_2O and 88–202 ppm S. Closer inspection reveals that the F/Cl ratio estimated for the CE5 basalt mantle source is lower in comparison to the ratios for depleted Earth mantle and primitive lunar mantle by Ni et al. (2019), while the H_2O content estimated is at the higher end of the estimates from McCubbin et al. (2023).

To sum up, the two most significant factors affecting the volatile estimations in the CE5 basalt mantle source are apatite composition and the petrogenetic model for CE5 basalt. To be certain whether the relatively low F/Cl characteristics of apatite composition imply an enriched CE5 basalt mantle source as suggested by the set of higher estimations, requires better constraints on the petrogenetic model for CE5 basalt, which is still under debate (Tian et al., 2021; Zong et al., 2022; Haupt et al., 2023; Z. Wang et al., 2024; C. Wang et al., 2024). Lower degrees of partial melting proposed in the model of Tian et al. (2021) result in a higher degree of enrichment of Cl relative to F, which could be responsible for the lower F/Cl ratios in the CE5 parental melt compared to Apollo high-Ti and low-Ti basalts. These considerations also apply to lunar meteorites with evolved bulk composition and apatite compositions similar to what we report here for CE5 basalt.

5. Conclusions

Through a detailed petrogenetic study of apatite in CE5 basalt, we are able to gain better understanding of the apatite compositional evolution, and also draw inferences on the volatile budget in the parental melt and the lunar mantle based on the earliest crystallized apatite compositions. Being a late crystallizing mineral and displaying compositional variations due to the interplay of fractional crystallization and degassing, it is not a simple task to relate the volatile compositions of apatite to that in the parental melt. Understanding the petrogenesis of CE5 basalt is further required to translate the volatile estimations for the parental melt to volatile abundances in the mantle source. Although we have not reached a finite conclusion regarding the volatile composition of the CE5 basalt mantle source, what we have learned through such an exercise contributes to the general understanding of lunar apatite compositional variation, the late-stage evolution of lunar basalt and volatile estimations for the lunar mantle. The main findings of this study are summarized below.

1) Melt immiscibility enhanced the enrichment of incompatible elements in the immiscible mafic melt and promoted the saturation of phosphates, hyalophane and Zr-bearing minerals.

2) The evolution of lunar basalt may firstly reach apatite saturation, then devolatilization and increase of P_2O_5 activity may result in merrillite saturation at a later stage.
3) The difference in zoning patterns, and general inter-grain variations of shapes, sizes and incompatible element concentrations suggest different generations of apatite crystallization.
4) Apatite compositions reported here show relatively low F and high Cl characteristics (0.97–2.47 wt% F and 0.24–1.09 wt% Cl), which are distinct from previously reported apatite compositions for Apollo high-Ti and low-Ti basalts, but show similarities to the apatite compositions from meteorites LAP 04841 and MIL 05035. Apatite Cl and S contents show a positive correlation with S contents up to ~ 3000 ppm, much higher than previous reports for Apollo samples (up to ~ 600 ppm).
5) The immiscible mafic and felsic melts preserved in olivine and ilmenite contain on average ~ 2500 and ~ 500 ppm S, respectively. The late-stage felsic melts in the mesostasis contain low S contents < 100 ppm. All these values are shown to represent S content in melt at sulfide saturation, i.e., SCSS.
6) The decreasing F and increasing Cl and S contents in the FC-dominated zoning profile can be explained by employing the model of Boyce et al. (2014). Degassing loss of H_2O and high S content in melt (likely at sulfide saturation) are required to explain the high Cl and S contents observed in our sample.
7) Based on the core compositions of the FC-dominated zoning profile, F, Cl and H_2O contents in the parental melt are estimated to be ~ 72 ± 21, ~43 ± 14 and ~ 1576 ± 518 ppm, respectively. Volatile estimates for the lunar mantle are similar to those for the depleted Earth mantle and primitive lunar mantle or 5–10 times lower depending on the petrogenetic model for CE5 basalt selected.

CRediT authorship contribution statement

Huijuan Li: Writing – review & editing, Writing – original draft, Visualization, Validation, Methodology, Investigation, Formal analysis, Data curation, Conceptualization. **Zilong Wang:** Writing – review & editing, Validation, Methodology, Investigation, Formal analysis, Data curation. **Zhenyu Chen:** Methodology, Formal analysis. **Wei Tian:** Resources, Project administration, Methodology, Investigation, Funding acquisition. **Wei-(RZ) Wang:** Resources, Project administration, Methodology, Investigation, Funding acquisition. **Guibin Zhang:** Resources, Project administration, Conceptualization. **Lifei Zhang:** Validation, Supervision, Resources, Project administration, Funding acquisition, Conceptualization.

Data availability

Data are available through Mendeley Data at https://doi.org/10.17632/k37fwxgtvw.1.

Declaration of competing interest

The authors declare that they have no known competing financial interests or personal relationships that could have appeared to influence the work reported in this paper.

Acknowledgements

Constructive suggestions and comments from the three reviewers have guided the revision of this manuscript. The fair yet sympathetic evaluation provided by editor Mahesh Anand is particularly appreciated. We thank the China National Space Administration (CNSA) for providing the Chang'E-5 samples. Jesse Jones is thanked for helpful discussions and suggestions on the presentation of the paper. Huijuan Li acknowledges financial support from the Center for High Pressure Science and Technology Advanced Research (HPSTAR) and also financial support received while working at Peking University from the National Key Research and Development Program of China through grant 2019YFA0708501 awarded to Lifei Zhang. Zilong Wang and Wei Tian acknowledge support from the National Natural Science Foundation of China through grant 42272348 awarded to Wei Tian.

Appendix A. Supplementary material

Readers can find representative phase compositions in association with mesostasis (Table S1); apatite compositions from individual analytical points (Table S2); late-stage felsic melt compositions from clast 1 (Table S3); and compositions for melt inclusions and late-stage felsic melts from clast 2 (Table S4).

Supplementary material to this article can be found online at https://doi.org/10.1016/j.gca.2024.09.002.

References

Aiuppa, A., 2009. Degassing of halogens from basaltic volcanism: insights from volcanic gas observations. Chem. Geol. 263, 99–109.

Anand, M., Taylor, L.A., Floss, C., Neal, C.R., Terada, K., Tanikawa, S., 2006. Petrology and geochemistry of LaPaz Icefield 02205: A new unique low-Ti mare-basalt meteorite. Geochim. Cosmochim. Acta 70, 246–264.

Barnes, J.J., Franchi, I.A., Anand, M., Tartèse, R., Starkey, N.A., Koike, M., Sano, Y., Russell, S.S., 2013. Accurate and precise measurements of the D/H ratio and hydroxyl content in lunar apatites using NanoSIMS. Chem. Geol. 337–338, 48–55.

Barnes, J.J., Tartèse, R., Anand, M., McCubbin, F.M., Neal, C.R., Franchi, I.A., 2016. Early degassing of lunar urKREEP by crust-breaching impact(s). Earth Planet. Sci. Lett. 447, 84–94.

Barnes, J.J., Franchi, I.A., McCubbin, F.M., Anand, M., 2019. Multiple reservoirs of volatiles in the Moon revealed by the isotopic composition of chlorine in lunar basalts. Geochim. Cosmochim. Acta 266, 144–162.

Barrett, T.J., Robinson, K.L., Barnes, J.J., Jeffrey, T.G., Nagashima, K., Huss, G.R., Franchi, I.A., Anand, M., Kring, D.A., 2023. Deciphering the origin(s) of H and Cl in Apollo 15 quartz monzodiorites: Evidence for multiple processes and reservoirs. Geochim. Cosmochim. Acta 358, 192–206.

Beyer, C., Klemme, S., Wiedenbeck, M., Stracke, A., Vollmer, C., 2012. Fluorine in nominally fluorine-free mantle minerals: Experimental partitioning of F between olivine, orthopyroxene and silicate melts with implications for magmatic processes. Earth Planet. Sci. Lett. 337–338, 1–9.

Boyce, J.W., Liu, Y., Rossman, G.R., Guan, Y., Eiler, J.M., Stolper, E.M., Taylor, L.a., 2010. Lunar apatite with terrestrial volatile abundances. Nature 466, 466–469.

Boyce, J.W., Tomlinson, S.M., McCubbin, F.M., Greenwood, J.P., Treiman, A.H., 2014. The lunar apatite paradox. Science 344, 400–402.

Boyce, J.W., Treiman, A.H., Guan, Y., Ma, C., Eiler, J.M., Gross, J., Greenwood, J.P., Stolper, E.M., 2015. The chlorine isotope fingerprint of the lunar magma ocean. Sci. Adv. 1, e1500380.

Brounce, M., Boyce, J., McCubbin, F.M., Humphreys, J., Reppart, J., Stolper, E., Eiler, J., 2019. The oxidation state of sulfur in lunar apatite. Am. Mineral. 104, 307–312.

Brounce, M., Boyce, J.W., Barnes, J., McCubbin, F.M., 2020. Sulfur in the apollo lunar basalts and implications for future sample-return missions. Elements 16, 361–362.

Che, X., Nemchin, A., Liu, D., Long, T., Wang, C., Norman, M.D., Joy, K.H., Tartese, R., Head, J., Jolliff, B., Snape, J.F., Neal, C.R., Whitehouse, M.J., Crow, C., Benedix, G., Jourdan, F., Yang, Z., Yang, C., Liu, J., Xie, S., Bao, Z., Fan, R., Li, D., Li, Z., Webb, S. G., 2021. Age and composition of young basalts on the Moon, measured from samples returned by Chang'e-5. Science 374, 887–890.

Chen, Y., Zhang, Y., Liu, Y., Guan, Y., Eiler, J., Stolper, E.M., 2015. Water, fluorine, and sulfur concentrations in the lunar mantle. Earth Planet. Sci. Lett. 427, 37–46.

Day, J.M.D., Taylor, L.A., Floss, C., Patchen, A.D., Schnare, D.W., Pearson, D.G., 2006. Comparative petrology, geochemistry, and petrogenesis of evolved, low-Ti lunar mare basalt meteorites from the LaPaz Icefield, Antarctica. *Geochim. Cosmochim. Acta* 70, 1581–1600.

Ding, S., Hough, T., Dasgupta, R., 2018. New high pressure experiments on sulfide saturation of high-FeO*basalts with variable TiO2contents – Implications for the sulfur inventory of the lunar interior. Geochim. Cosmochim. Acta 222, 319–339.

Elardo, S.M., Shearer, C.K., Vander Kaaden, K.E., McCubbin, F.M., Bell, A.S., 2015. Petrogenesis of primitive and evolved basalts in a cooling Moon: Experimental constraints from the youngest known lunar magmas. Earth Planet. Sci. Lett. 422, 126–137.

Gargano, A., Sharp, Z., Shearer, C., Simon, J.I., Halliday, A., Buckley, W., 2020. The Cl isotope composition and halogen contents of Apollo-return samples. Proc. Natl. Acad. Sci. U. S. A. 117, 23418–23425.

Goldoff, B., Webster, J.D., Harlov, D.E., 2012. Characterization of fluor-chlorapatites by electron probe microanalysis with a focus on time-dependent intensity variation of halogens. Am. Mineral. 97, 1103–1115.

Greenwood, J.P., Itoh, S., Sakamoto, N., Warren, P., Taylor, L., Yurimoto, H., 2011. Hydrogen isotope ratios in lunar rocks indicate delivery of cometary water to the Moon. Nat. Geosci. 4, 79–82.

Gross, J., Filiberto, J., Bell, A.S., 2013. Water in the martian interior: Evidence for terrestrial MORB mantle-like volatile contents from hydroxyl-rich apatite in olivine–phyric shergottite NWA 6234. Earth Planet. Sci. Lett. 369–370, 120–128.

Haupt, C.P., Renggli, C.J., Klaver, M., Steenstra, E.S., Berndt, J., Rohrbach, A., Klemme, S., 2023. Experimental and petrological investigations into the origin of the lunar Chang'e 5 basalts. Icarus 402, 115625.

Hauri, E., Gaetani, G., Green, T., 2006. Partitioning of water during melting of the Earth's upper mantle at H2O-undersaturated conditions. Earth Planet. Sci. Lett. 248, 715–734.

Hauri, E.H., Weinreich, T., Saal, A.E., Rutherford, M.C., Van Orman, J.A., 2011. High pre-eruptive water contents preserved in lunar melt inclusions. Science 333, 213–215.

He, Q., Li, Y., Baziotis, I., Qian, Y., Xiao, L., Wang, Z., Zhang, W., Luo, B., Neal, C.R., Day, J.M.D., Pan, F., She, Z., Wu, X., Hu, Z., Zong, K., Wang, L., 2022. Detailed petrogenesis of the unsampled Oceanus Procellarum: The case of the Chang'e-5 mare basalts. Icarus 383, 115082.

Hill, E., Taylor, L.A., Floss, C., Liu, Y., 2009. Lunar meteorite LaPaz Icefield 04841: Petrology, texture, and impact-shock effects of a low-Ti mare basalt. Meteorit. Planet. Sci. 44, 87–94.

Hu, S., Huicun, H.e., Ji, J., Lin, Y., Hui, H., Anand, M., Tartèse, R., Yan, Y., Hao, J., Li, R., Gu, L., Guo, Q., Huaiyu, H.e., Ouyang, Z., 2021. A dry lunar mantle reservoir for young mare basalts of chang'e-5. Nature 600, 49–53.

Ji, J., He Huicun, H.S., Lin, Y., Hui, H., Hao, J., Li, R., Yang, W., Yan, Y., Tian, H., Zhang, C., Anand, M., Tartèse, R., Gu, L., Li, J., Zhang, D., Mao, Q., Jia, L., Chen, Y., Wu, S., Wang, H., Huaiyu, H.e., Li, X., Wu, F., 2022. Magmatic chlorine isotope fractionation recorded in apatite from chang'e-5 basalts. Earth Planet. Sci. Lett. 591, 117636.

Jolliff, B.L., Haskin, L.A., Colson, R.O., Wadhwa, M., 1993. Partitioning in REE-saturating minerals: theory, experiment, and modelling of whitlockite, apatite, and evolution of lunar residual magmas. Geochim. Cosmochim. Acta 57, 4069–4094.

Jolliff, B.L., Hughes, J.M., Freeman, J.J., Zeigler, R.A., 2006. Crystal chemistry of lunar merrillite and comparison to other meteoritic and planetary suites of whitlockite and merrillite. Am. Mineral. 91, 1583–1595.

Joy, K.H., Crawford, I.A., Downes, H., Russell, S.S., Kearsley, A.T., 2006. A petrological, mineralogical, and chemical analysis of the lunar mare basalt meteorite LaPaz Icefield 02205, 02224, and 02226. Meteorit. Planet. Sci. 41, 1003–1025.

Joy, K.H., Crawford, I.A., Anand, M., Greenwood, R.C., Franchi, I.A., Russell, S.S., 2008. The petrology and geochemistry of Miller Range 05035: A new lunar gabbroic meteorite. Geochim. Cosmochim. Acta 72, 3822–3844.

Konecke, B.A., Fiege, A., Simon, A.C., Holtz, F., 2017. Cryptic metasomatism during late-stage lunar magmatism implicated by sulfur in apatite. Geology 45, 739–742.

Konecke, B.A., Fiege, A., Simon, A.C., Linsler, S., Holtz, F., 2019. An experimental calibration of a sulfur-in-apatite oxybarometer for mafic systems. Geochim. Cosmochim. Acta 265, 242–258.

Li, W., Costa, F., 2020. A thermodynamic model for F-Cl-OH partitioning between silicate melts and apatite including non-ideal mixing with application to constraining melt volatile budgets. Geochim. Cosmochim. Acta 269, 203–222.

Li, H., Hermann, J., 2015. Apatite as an indicator of fluid salinity: An experimental study of chlorine and fluorine partitioning in subducted sediments. Geochim. Cosmochim. Acta 166, 267–297.

Li, H., Hermann, J., 2017. The effect of fluorine and chlorine on trace element partitioning between apatite and sediment melt at subduction zone conditions. Chem. Geol. 473, 55–73.

Li, Q.-L., Zhou, Q., Liu, Y., Xiao, Z., Lin, Y., Li, J.-H., Ma, H.-X., Tang, G.-Q., Guo, S., Tang, X., Yuan, J.-Y., Li, J., Wu, F.-Y., Ouyang, Z., Li, C., Li, X.-H., 2021. Two-billion-year-old volcanism on the Moon from Chang'e-5 basalts. Nature 600, 54–58.

Liu, Y., Floss, C., Day, J.M.D., Hill, E., Taylor, L.A., 2009. Petrogenesis of lunar mare basalt meteorite miller range 05035. Meteorit. Planet. Sci. 44, 261–284.

Liu, X., Hao, J., Li, R., He, Y., Tian, H., Hu, S., Li, J., Gu, L., Yang, W., Lin, Y., 2022. Sulfur isotopic fractionation of the youngest chang'e-5 basalts: constraints on the magma degassing and geochemical features of the mantle source. *Geophys. Res. Lett.* 49.

Liu, Y., Samaha, N.T., Baker, D.R., 2007. Sulfur concentration at sulfide saturation (SCSS) in magmatic silicate melts. Geochim. Cosmochim. Acta 71, 1783–1799.

Martínez, M., Shearer, C.K., Brearley, A.J., 2023. Nanostructural domains in martian apatites that record primary subsolidus exsolution of halogens: Insights into nakhlite petrogenesis. Am. Mineral. 108, 2024–2042.

McCubbin, F.M., Hauri, E.H., Elardo, S.M., Vander Kaaden, K.E., Wang, J., Shearer, C.K., 2012. Hydrous melting of the martian mantle produced both depleted and enriched shergottites. Geology 40, 683–686.

McCubbin, F.M., Boyce, J.W., Srinivasan, P., Santos, A.R., Elardo, S.M., Filiberto, J., Steele, A., Shearer, C.K., 2016. Heterogeneous distribution of H2O in the Martian interior: Implications for the abundance of H2O in depleted and enriched mantle sources. Meteorit. Planet. Sci. 51, 2036–2060.

McCubbin, F.M., Barnes, J.J., Ni, P., Hui, H., Klima, R.L., Burney, D., Day, J.M.D., Magna, T., Boyce, J.W., Tartèse, R., Kaaden, K.E., Vander, S.E., Elardo, S.M., Zeigler, R.A., Anand, M., Liu, Y., 2023. Endogenous lunar volatiles. Rev. Mineral. Geochemistry 89, 729–786.

McCubbin, F.M., Ustunisik, G., 2018. Experimental investigation of F and Cl partitioning between apatite and Fe-rich basaltic melt at 0 GPa and 950–1050 °c: Evidence for steric controls on apatite-melt exchange equilibria in OH-poor apatite. Am. Mineral. 103, 1455–1467.

McCubbin, F.M., Steele, A., Hauri, E.H., Nekvasil, H., Yamashita, S., Hemley, R.J., 2010a. Nominally hydrous magmatism on the Moon. Proc. Natl. Acad. Sci. 107, 11223–11228.

McCubbin, F.M., Steele, A., Nekvasil, H., Schnieders, A., Rose, T., Fries, M., Carpenter, P. K., Jolliff, B.L., 2010b. Detection of structurally bound hydroxyl in fluorapatite from Apollo Mare basalt 15058,128 using TOF-SIMS. Am. Mineral. 95, 1141–1150.

McCubbin, F.M., Jolliff, B.L., Nekvasil, H., Carpenter, P.K., Zeigler, R.a., Steele, A., Elardo, S.M., Lindsley, D.H., 2011. Fluorine and chlorine abundances in lunar apatite: Implications for heterogeneous distributions of magmatic volatiles in the lunar interior. Geochim. Cosmochim. Acta 75, 5073–5093.

McCubbin, F.M., Vander Kaaden, K.E., Tartèse, R., Boyce, J.W., Mikhail, S., Whitson, E. S., Bell, A.S., Anand, M., Franchi, I.A., Wang, J., Hauri, E.H., 2015a. Experimental investigation of F, Cl, and OH partitioning between apatite and Fe-rich basaltic melt at 1.0–1.2 GPa and 950–1000 °C. Am. Mineral. 100, 1790–1802.

McCubbin, F.M., Vander Kaaden, K.E., Tartèse, R., Klima, R.L., Liu, Y., Mortimer, J., Barnes, J.J., Shearer, C.K., Treiman, A.H., Lawrence, D.J., Elardo, S.M., Hurley, D. M., Boyce, J.W., Anand, M., 2015b. Magmatic volatiles (H, C, N, F, S, Cl) in the lunar mantle, crust, and regolith: Abundances, distributions, processes, and reservoirs. Am. Mineral. 100, 1668–1707.

Mollo, S., Hammer, J.E., 2017. Dynamic crystallization in magmas. In: *Mineral reaction kinetics: Microstructures, textures, chemical and isotopic signatures* Mineralogical Society of Great Britain & Ireland, pp. 378–418.

Ni, P., Zhang, Y., Chen, S., Gagnon, J., 2019. A melt inclusion study on volatile abundances in the lunar mantle. Geochim. Cosmochim. Acta 249, 17–41.

O'Leary, J.A., Gaetani, G.A., Hauri, E.H., 2010. The effect of tetrahedral Al3+ on the partitioning of water between clinopyroxene and silicate melt. Earth Planet. Sci. Lett. 297, 111–120.

O'Neill, H.S.C., 2021. The thermodynamic controls on sulfide saturation in silicate melts with application to ocean floor basalts. American geophysical union, pp. 177–213.

Pan, Y., Fleet, M.E., 2002. Compositions of the apatite-group minerals: substitution mechanisms and controlling factors. Rev. Mineral. Geochemistry 48, 13–49.

Patiño Douce, A.E., Roden, M., 2006. Apatite as a probe of halogen and water fugacities in the terrestrial planets. Geochim. Cosmochim. Acta 70, 3173–3196.

Patiño, A.E., Roden, M.F., Chaumba, J., Fleisher, C., Yogodzinski, G., 2011. Compositional variability of terrestrial mantle apatites, thermodynamic modeling of apatite volatile contents, and the halogen and water budgets of planetary mantles. Chem. Geol. 288, 14–31.

Pernet-Fisher, J.F., Howarth, G.H., Liu, Y., Chen, Y., Taylor, L.A., 2014. Estimating the lunar mantle water budget from phosphates: Complications associated with silicate-liquid-immiscibility. Geochim. Cosmochim. Acta 144, 326–341.

Potts, N.J., Barnes, J.J., Tartèse, R., Franchi, I.A., Anand, M., 2018. Chlorine isotopic compositions of apatite in Apollo 14 rocks: Evidence for widespread vapor-phase metasomatism on the lunar nearside ~4 billion years ago. Geochim. Cosmochim. Acta 230, 46–59.

Potts, N.J., Bromiley, G.D., Brooker, R.A., 2021. An experimental investigation of F, Cl and H2O mineral-melt partitioning in a reduced, model lunar system. Geochim. Cosmochim. Acta 294, 232–254.

Putirka, K.D., 2008. Thermometers and barometers for volcanic systems. Rev. Mineral. Geochemistry 69, 61–120.

Qian, Y.Q., Xiao, L., Zhao, S.Y., Zhao, J.N., Huang, J., Flahaut, J., Martinot, M., Head, J. W., Hiesinger, H., Wang, G.X., 2018. Geology and scientific significance of the rümker region in northern oceanus procellarum: china's chang'E-5 landing region. J. Geophys. Res. Planets 123, 1407–1430.

Robinson, K.L., Taylor, G.J., 2014. Heterogeneous distribution of water in the Moon. Nat. Geosci. 7, 401–408.

Roedder, E., Weiblen, P.W., 1970. Lunar petrology of silicate melt inclusions, Apollo 11 rocks. Pergammon Press, New YorkHouston, TX, p. 801.

Roedder, E., Weiblen, P.W., 1971. Petrology of silicate melt inclusions, Apollo 11 and Apollo 12 and terrestrial equivalents. In: Proceedings of the Lunar Science Conference, p. 507.

Rosenthal, A., Hauri, E.H., Hirschmann, M.M., 2015. Experimental determination of C, F, and H partitioning between mantle minerals and carbonated basalt, CO2/Ba and CO2/Nb systematics of partial melting, and the CO2 contents of basaltic source regions. Earth Planet. Sci. Lett. 412, 77–87.

Saal, A.E., Hauri, E.H., Langmuir, C.H., Perfit, M.R., 2002. Vapour undersaturation in primitive mid-ocean-ridge basalt and the volatile content of Earth's upper mantle. Nature 419, 451–455.

Saal, A.E., Hauri, E.H., Van Orman, J.A., Rutherford, M.J., 2013. Hydrogen isotopes in lunar volcanic glasses and melt inclusions reveal a carbonaceous chondrite heritage. Science 340, 1317–1320.

Salters, V.J.M., Stracke, A., 2004. Composition of the depleted mantle. Geochemistry, Geophys. Geosystems. 5, Q05004.

Sharp, Z.D., Shearer, C.K., McKeegan, K.D., Barnes, J.D., Wang, Y.Q., 2010. The chlorine isotope composition of the moon and implications for an anhydrous mantle. Science 329, 1050–1053.

Shearer, C.K., Papike, J.J., Spilde, M.N., 2001. Trace-element partitioning between immiscible lunar melts: An example from naturally occurring lunar melt inclusions. Am. Mineral. 86, 238–246.

Shima, H., Naldrett, A.J., 1975. Solubility of sulfur in an ultramafic melt and the relevance of the system Fe-S-O. Econ. Geol. 70, 960–967.

Singer, J.A., Greenwood, J.P., Itoh, S., Sakamoto, N., Yurimoto, H., 2017. Evidence for the solar wind in lunar magmas: A study of slowly cooled samples of the Apollo 12 olivine basalt suite. Geochem. J. 51, 95–104.

Snyder, G.A., Taylor, L.A., Crozaz, G., 1993. Rare earth element selenochemistry of immiscible liquids and zircon at Apollo 14: An ion probe study of evolved rocks on the Moon. Geochim. Cosmochim. Acta 57, 1143–1149.

Stadermann, A.C., Jolliff, B.L., Krawczynski, M.J., Hamilton, C.W., Barnes, J.J., 2022. Analysis and experimental investigation of Apollo sample 12032,366–18, a chemically evolved basalt from the Moon. Meteorit. Planet. Sci. 57, 794–816.

Stephant, A., Anand, M., Zhao, X., Chan, Q.H.S., Bonifacie, M., Franchi, I.A., 2019. The chlorine isotopic composition of the Moon: Insights from melt inclusions. Earth Planet. Sci. Lett. 523, 115715.

Stephant, A., Anand, M., Tartèse, R., Zhao, X., Degli-Alessandrini, G., Franchi, I.A., 2020. The hydrogen isotopic composition of lunar melt inclusions: An interplay of complex magmatic and secondary processes. Geochim. Cosmochim. Acta 284, 196–221.

Stormer, J.C., Pierson, M.L., Tacker, R.C., 1993. Variation of F and Cl X-ray intensity due to anisotropic diffusion in apatite during electron microprobe analysis. Am. Mineral. 78, 641–648.

Su, B., Yuan, J., Chen, Y., Yang, W., Mitchell, R.N., Hui, H., Wang, H., Tian, H., Li, X., Wu, F., 2022. Fusible mantle cumulates trigger young mare volcanism on the cooling Moon. Sci. Adv. 8, 1–8.

Tartèse, R., Anand, M., Barnes, J.J., Starkey, N.a., Franchi, I.a., Sano, Y., 2013. The abundance, distribution, and isotopic composition of Hydrogen in the Moon as revealed by basaltic lunar samples: Implications for the volatile inventory of the Moon. Geochim. Cosmochim. Acta 122, 58–74.

Tartèse, R., Anand, M., Joy, K.H., Franchi, I.A., 2014a. H and Cl isotope systematics of apatite in brecciated lunar meteorites Northwest Africa 4472, Northwest Africa 773, Sayh al Uhaymir 169, and Kalahari 009. Meteorit. Planet. Sci. 49, 2266–2289.

Tartèse, R., Anand, M., McCubbin, F.M., Elardo, S.M., Shearer, C.K., Franchi, I.A., 2014b. Apatites in lunar KREEP basalts: The missing link to understanding the H isotope systematics of the Moon. Geology 42, 363–366.

Tian, H.-C., Wang, H., Chen, Y., Yang, W., Zhou, Q., Zhang, C., Lin, H.-L., Huang, C., Wu, S.-T., Jia, L.-H., Xu, L., Zhang, D., Li, X.-G., Chang, R., Yang, Y.-H., Xie, L.-W., Zhang, D.-P., Zhang, G.-L., Yang, S.-H., Wu, F.-Y., 2021. Non-KREEP origin for chang'e-5 basalts in the procellarum KREEP terrane. Nature 600, 59–63.

Wang, Y., Hsu, W., Guan, Y., 2019. An extremely heavy chlorine reservoir in the Moon: Insights from the apatite in lunar meteorites. Sci. Rep. 9, 1–8.

Wang, Z., Wang, W.R.Z., Tian, W., Li, H., Qian, Y., Pei, J., Chen, Z., Wang, D., Liu, P., Fa, W., Wu, J., Bao, H., 2023. Cooling rate of clinopyroxene reveals the thickness and effusion volume of Chang'E-5 basaltic flow units. Icarus 394, 115406.

Wang, C., Xu, Y.-G., Zhang, L., Chen, Z., Xia, X., Lin, M., Guo, F., 2024a. A shallow (<100 km) ilmenite-bearing pyroxenitic source for young lunar volcanism. Earth Planet. Sci. Lett. 639, 118770.

Wang, Z., Zong, K., Li, Y., Li, J., He, Q., Zou, Z., Becker, H., Moynier, F., Day, J.M.D., Zhang, W., Qian, Y., Xiao, L., Hu, Z., She, Z., Hui, H., Wu, X., Liu, Y., 2024b. Young KREEP-like mare volcanism from oceanus procellarum. Geochim. Cosmochim. Acta 373, 17–34.

Wetzel, D.T., Hauri, E.H., Saal, A.E., Rutherford, M.J., 2015. Carbon content and degassing history of the lunar volcanic glasses. Nat. Geosci. 8, 755–758.

Young E. J., Myers A. T., Munson W. L. and Conklin N. M. (1969) Mineralogy and geochemistry of fluorapatite from Cero de Mercado, Durango, Mexico. *U.S. Geol. Surv. Prof. Pap.* **650-D**, D84–D93.

Zeng, X., Joy, K.H., Li, S., Lin, Y., Wang, N., Li, X., Li, Y., Hao, J., Liu, J., Wang, S., 2020. Oldest immiscible silica-rich melt on the moon recorded in a ~4.38 ga zircon. Geophys. Res. Lett. 47, 1–10.

Zhang, Y., 2020. H 2 O and other volatiles in the moon, 50 years and on. ACS Earth Sp. Chem. 4, 1480–1499.

Zong, K., Wang, Z., Li, J., He, Q., Li, Y., Becker, H., Zhang, W., Hu, Z., He, T., Cao, K., She, Z., Wu, X., Xiao, L., Liu, Y., 2022. Bulk compositions of the Chang'E-5 lunar soil: Insights into chemical homogeneity, exotic addition, and origin of landing site basalts. Geochim. Cosmochim. Acta 335, 284–296.